Inorganic Chemistry

Article

pubs.acs.org/IC

Observation of Ferromagnetic Exchange, Spin Crossover, Reductively Induced Oxidation, and Field-Induced Slow Magnetic Relaxation in Monomeric Cobalt Nitroxides

Ian A. Gass,[†] Subrata Tewary,[#] Ayman Nafady,[▽] Nicholas. F. Chilton,[†] Christopher J. Gartshore,[†] Mousa Asadi,[†] David W. Lupton,[†] Boujemaa Moubaraki,[†] Alan M. Bond,[†] John F. Boas,[‡] Si-Xuan Guo,[†] Gopalan Rajaraman,[#] and Keith S. Murray*[,†]

[†]School of Chemistry, Monash University, Clayton, Victoria 3800, Australia

[‡]School of Physics, Monash University, Clayton, Victoria 3800, Australia

[§]School of Chemistry, University of Melbourne, Victoria 3010, Australia

[#]Department of Chemistry, Indian Institute of Technology—Bombay, Powai, Mumbai, India

[▽]Department of Chemistry, King Saud University, P.O. Box 2455, Riyadh−11451, Kingdom of Saudi Arabia

Supporting Information

ABSTRACT: The reaction of $[Co^{II}(NO_3)_2]\cdot 6H_2O$ with the nitroxide radical, 4-dimethyl-2,2-di(2-pyridyl) oxazolidine-*N*-oxide ($L^{\bullet}$), produces the mononuclear transition-metal complex $[Co^{II}(L^{\bullet})_2](NO_3)_2$ (**1**), which has been investigated using temperature-dependent magnetic susceptibility, electron paramagnetic resonance (EPR) spectroscopy, electrochemistry, density functional theory (DFT) calculations, and variable-temperature X-ray structure analysis. Magnetic susceptibility measurements and X-ray diffraction (XRD) analysis reveal a central low-spin octahedral Co^{2+} ion with both ligands in the neutral radical form ($L^{\bullet}$) forming a linear $L^{\bullet}\cdots Co(II)\cdots L^{\bullet}$ arrangement. This shows a host of interesting magnetic properties including strong cobalt-radical and radical−radical intramolecular ferromagnetic interactions stabilizing a $S = {}^3/_2$ ground state, a thermally induced spin crossover transition above 200 K and field-induced slow magnetic relaxation. This is supported by variable-temperature EPR spectra, which suggest that **1** has a positive *D* value and nonzero *E* values, suggesting the possibility of a field-induced transverse anisotropy barrier. DFT calculations support the parallel alignment of the two radical π^*_{NO} orbitals with a small orbital overlap leading to radical−radical ferromagnetic interactions while the cobalt-radical interaction is computed to be strong and ferromagnetic. In the high-spin (HS) case, the DFT calculations predict a weak antiferromagnetic cobalt-radical interaction, whereas the radical−radical interaction is computed to be large and ferromagnetic. The monocationic complex $[Co^{III}(L^{-})_2](BPh_4)$ (**2**) is formed by a rare, reductively induced oxidation of the Co center and has been fully characterized by X-ray structure analysis and magnetic measurements revealing a diamagnetic ground state. Electrochemical studies on **1** and **2** revealed common Co-redox intermediates and the proposed mechanism is compared and contrasted with that of the Fe analogues.

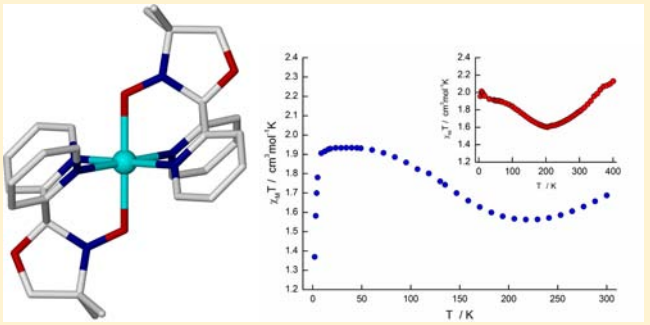

1. INTRODUCTION

Metal complexes involving redox active ligands such as α-dithiolenes,[1] α-diimines,[2] and 1,2-dioxolenes,[3] exhibit non-innocent behavior and have been studied extensively to gain a fuller understanding of their electronic structure by assignment of the "correct" oxidation state of the metal, identification of the nature of the ligands involved, and determination of any redox intermediates via a combination of electrochemical, spectroscopic, magnetic, and computational studies. Such ligands are also biologically relevant, where, for example, 1,2-dioxolenes are thought to chelate to the nonheme iron center in catechol dioxygenases[4] and α-dithiolene groups are present in the cofactor molybdopterin found in a variety of metalloenzymes.[5] One-electron redox processes in such ligands invariably leads to the generation of radical species, which, when coupled with redox-active metal centers, can show strong magnetic exchange[6] and electronic delocalization,[7] resulting in ambiguous electronic structures.

Studies on redox active nitroxide (formally aminoxyl) radical species coordinated to Cu(II) offered a great model system to examine the direct exchange between the $d_{x^2-y^2}$ magnetic orbital on the Cu(II) and the π* molecular orbital of the nitroxide NO group. Axial coordination of the nitroxide NO group to Cu(II)

Received: March 5, 2013
Published: June 18, 2013

   dx.doi.org/10.1021/ic400565h | *Inorg. Chem.* 2013, 52, 7557−7572

has been reported to induce moderate ferromagnetic interactions while equatorial coordination results in strong antiferromagnetic exchange.[6c−e] These interactions have been rationalized by an orbital overlap argument where significant overlap between the magnetic orbital(s) leads to antiferromagnetic exchange whereas an orthogonal arrangement of the magnetic orbital(s) leads to a ferromagnetic interaction. This degree of overlap which contributes to the antiferromagnetic component of the exchange is particularly sensitive to the Euler angles ψ and θ when the nitroxide is equatorially bound while in the axially bound case for a given θ angle the largest overlap is when either ψ is close to 90° and θ is close to 0° or 90° or when ψ is close to 0° and θ is close to 45°. In each case, the magnitude of the exchange is related to the $M^{n+}-O_{nitroxide}$ bond distances.[8] However Luneau and co-workers have reported ferromagnetic interactions in equatorially bound Cu(II) nitroxides,[9] the axially bound Cu(II) nitroxide analogue of the complexes reported here shows antiferromagnetic interactions,[10] and large antiferromagnetic interactions were found in $Mn(hfac)_2(proxyl)_2$ (proxyl = 2,2,5,5-tetramethylpyrrolidyl-1-oxy) stabilizing a $S = {}^3/_2$ ground state.[11] Clearly, the magnitude and type of exchange seen in such d-block metal nitroxides is therefore very sensitive to the geometrical arrangement of the bound nitroxide and subsequent overlap with the magnetic orbital(s) of the metal in question. Apart from the orientation of the radical coordination, this overlap is also highly dependent on the metal ion d-electron configurations. Metals exhibiting spin crossover, such as iron or cobalt, when coupled with coordinated radicals, can be ideal model systems to study how the metal-radical exchange interaction changes as the central metal ion undergoes a spin transition. This offers yet another other degree of freedom to fine-tune the magnetic coupling. In this regard, we have decided to investigate octahedral Co(II) nitroxides, which form a linear $L^{\bullet}-Co^{II}-L^{\bullet}$ exchange coupled "hybrid" system exhibiting a host of interesting magnetic and electronic properties, including spin crossover, ferromagnetic exchange, reductively induced oxidation, and field-induced slow magnetic relaxation, i.e., single-molecule magnetic behavior.

Coordinated 4,4-dimethyl-2,2-di(2-pyridyl) oxazolidine-*N*-oxide (Figure 1) exists in its neutral radical ($L^{\bullet}$) or

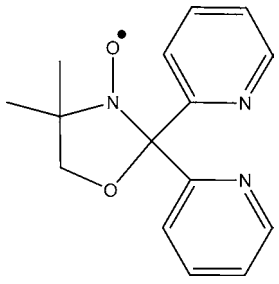

Figure 1. Structural formula of 4-dimethyl-2,2-di(2-pyridyl) oxazolidine *N*-oxide ($L^{\bullet}$).

hydroxylamino anionic form (L^-), as exemplified by our previous work on iron nitroxide chelates.[12] In that system, we postulated that the dication $[Fe^{II}(L^{\bullet})_2]^{2+}$ undergoes a one-electron reduction to form the intermediate $[Fe^{II}(L^{\bullet})(L^-)]^+$ in which an intramolecular electron transfer takes place to generate the monocationic species $[Fe^{III}(L^-)_2]^+$. In the $[Fe^{II}(L^{\bullet})_2]^{2+}$ dication, we observed a strong radical−radical antiferromagnetic coupling via the diamagnetic low-spin Fe(II) center ($J = -315$ cm^{-1}, using the spin Hamiltonian $-2J\mathbf{S}_1\cdot\mathbf{S}_2$). Here, we report on the synthesis of the congeners $[Co^{II}(L^{\bullet})_2](NO_3)_2$ (**1**) and $[Co^{III}(L^-)_2](BPh_4)$ (**2**) with the diamagnetic complex **2** formed by a reductively induced oxidation of the central cobalt ion, where the tetraphenylborate anion acts as a reducing agent. Complex **1** is a rare example of an octahedral Co(II) ion undergoing a spin transition and exhibiting ferromagnetic exchange between the coordinating nitroxide radicals and the central Co(II) ion in a linear $L^{\bullet}-Co^{II}-L^{\bullet}$ arrangement. This stabilizes an $S = {}^3/_2$ ground state, which shows slow magnetic relaxation (i.e., SMM) effects under an applied DC field. The low-temperature (and low-spin) region offers a unique model system to look at the direct exchange between the d_{z^2} magnetic orbital on the low-spin Co(II) ion and the π^* molecular orbital of the nitroxide NO group, providing an interesting comparison with previous studies on Cu(II) nitroxides where the magnetic orbital is usually $d_{x^2-y^2}$. It should be emphasized that these systems act as one-electron switches where a one-electron reduction of one of the ligands in solution results in a change in the iron system from the diamagnetic $[Fe^{II}(L^{\bullet})_2]^{2+}$ dication to the $S = {}^1/_2[Fe^{III}(L^-)_2]^+$ monocation, whereas in the cobalt system presented here, it changes from the $S = {}^3/_2[Co^{II}(L^{\bullet})_2]^{2+}$ dication to the diamagnetic $[Co^{III}(L^-)_2]^+$ monocation.

2. EXPERIMENTAL SECTION

2.1. General. 4,4-Dimethyl-2,2-di(2-pyridyl)oxazolidine *N*-oxide ($L^{\bullet}$) was synthesized as described previously.[12] All other reagents and solvents were of reagent-grade and used as-received. Microanalyses were performed by the Campbell Microanalytical Laboratory, Chemistry Department, University of Otago, Dunedin, New Zealand.

2.2. Syntheses. *$[Co^{II}(L^{\bullet})_2](NO_3)_2$ (**1**).* Ten milligrams (10 mg (0.037 mmol)) of 4,4-dimethyl-2,2-di(2-pyridyl) oxazolidine *N*-oxide ($L^{\bullet}$) and 5.4 mg (0.0186 mmol) of $Co^{II}(NO_3)_2\cdot 6H_2O$ were dissolved in 10 mL of acetonitrile. After 5 min of stirring, the resultant brown solution was filtered and diffused with Et_2O to produce X-ray quality crystals of **1** after 1 day. Yield: 7 mg (52.3%). Anal. Calcd (%) for **1**, $C_{30}H_{32}N_8O_{10}Co$: C, 49.8; H, 4.5; N, 15.5. Found: C, 50.0; H, 4.5; N, 15.6. IR (ATR cm^{-1}) 1600m, 1571w, 1465m, 1443m, 1409m, 1334s, 1303s, 1267s, 1155w, 1081m, 1022w, 999w, 928w, 807w, 773w.

*$[Co^{III}(L^-)_2](BPh_4)$ (**2**).* Ten milligrams (10 mg (0.037 mmol)) of 4,4-dimethyl-2,2-di(2-pyridyl) oxazolidine *N*-oxide ($L^{\bullet}$), 5.2 mg (0.0185 mmol) of $Co^{II}(SO_4)\cdot 7H_2O$, and 12.6 mg (0.037 mmol) of $Na(BPh_4)$ were dissolved in 10 mL of methanol. After 60 min of stirring, the resultant brown precipitate was dissolved in CH_2Cl_2, filtered, and diffused with Et_2O to produce X-ray quality crystals of **2** after 2 days. Yield: 5 mg (29.4%). Anal. Calcd (%) for **2**, $C_{54}H_{52}N_6O_4BCo$: C, 70.6; H, 5.7; N, 9.2. Found: C, 70.7; H, 5.8; N, 8.7. IR (ATR cm^{-1}): 3106s, 2974s, 2938w, 2882w, 1606m, 1578w, 1475m, 1461s, 1440s, 1429s, 1362w, 1269w, 1249m, 1219m, 1194w, 1157m, 1142m, 1075w, 1057w, 1030w, 987m, 954m, 941m, 874w, 851w, 767s, 730s, 701s, 682s, 667m, 653m, 606w.

2.3. Magnetic Susceptibility Measurements. Variable-temperature magnetic susceptibility measurements were performed on a Quantum Design MPMS 7T SQUID magnetometer from 1.8 K to 400 K were in applied DC fields ranging from 0 to 50 000 G. The SQUID magnetometer was calibrated using a standard palladium sample (Quantum Design) of accurately known magnetization or through the use of magnetochemical calibrants such as $CuSO_4\cdot 5H_2O$. Microcrystalline samples were dispersed in petroleum jelly in order to avoid torquing of the crystallites. Measurements up to 400 K were performed in a quartz tube. Alternating current (AC) magnetic susceptibility measurements were undertaken in oscillating fields of 3 G, frequencies in the range of 1−1500 Hz, and applied DC fields of 0, 2000, and 5000 G. The sample mulls were contained in a calibrated capsule held at the center of a drinking straw that was fixed at the end of the sample rod.

dx.doi.org/10.1021/ic400565h | *Inorg. Chem.* 2013, 52, 7557−7572

Table 1. Crystallographic Data for 1 (at 123, 273 and 353 K) and 2

	1·123 K	1·273 K	1·353 K	2
formula	$C_{30}H_{32}N_8O_{10}Co$	$C_{30}H_{32}N_8O_{10}Co$	$C_{30}H_{32}N_8O_{10}Co$	$C_{54}H_{52}N_6O_4BCo$
M_r	723.57	723.57	723.57	918.76
crystal system	monoclinic	monoclinic	monoclinic	monoclinic
space group	$P2_1/c$	$P2_1/c$	$P2_1/c$	$P2_1/c$
a (Å)	9.3825(10)	9.4853(5)	9.4854(13)	12.4781(14)
b (Å)	14.1324(17)	14.0862(6)	14.0059(17)	15.8940(18)
c (Å)	11.7395(15)	12.0890(6)	12.346(2)	23.212(3)
α (°)	90	90	90	90
β (°)	101.421(3)	101.495(5)	101.807(13)	104.920(4)
γ (°)	90	90	90	90
V (Å^3)	1525.8	1578.4	1605.5(4)	4448.3
T (K)	123(2)	273(2)	353(2)	123(2)
Z	2	2	2	4
ρ_{calcd} (g cm^{-3})	1.575	1.523	1.497	1.372
λ^a (Å)	0.71073	0.71073	0.71073	0.71073
number of ind. reflns	3483	3623	2815	10081
number of reflns with $I > 2\sigma(I)$	2499	2827	1693	5821
number of parameters	225	225	227	599
number of restraints	0	0	0	0
final $R1$, $wR2^b$ $[I > 2\sigma(I)]$	0.0665, 0.1749	0.0444, 0.1143	0.0584, 0.1281	0.0667, 0.1344
$R1$, $wR2^b$ all data	0.0945, 0.1925	0.0600, 0.1247	0.1121, 0.1582	0.1243, 0.1605
goodness of fit, GOF	1.015	1.036	1.052	0.999
largest residuals (e Å^{-3})	0.925, −0.516	0.580, −0.478	0.482, −0.357	0.834, −0.623

^{a}Graphite monochromators. $^b R1 = \sum ||F_o| - |F_c|| / \sum |F_o|$, $wR2 = \{\sum[w(F_o^2 \sum F_c^2)^2] / \sum[w(F_o^2)]\}^{1/2}$.

2.4. X-ray Crystallography. X-ray crystallographic measurements on **1** and **2** were performed at 123(2) K using a Bruker Smart Apex X8 diffractometer with Mo Kα radiation (λ = 0.7107 Å). Single crystals were mounted on a glass fiber using oil. Higher-temperature data collections for complex **1** were performed at 273 K and 353 K, using an Oxford Gemini Ultra diffractometer with Mo Kα radiation (λ = 0.7107 Å). Crystallographic data and refinement parameters for **1** and **2**, given in Table 1, were solved by direct methods (SHELXS-97), and refined (SHELXL-97) by full least-squares on all F^2 data.[13] In complex **1** (at all temperatures), the asymmetric unit contains half a monomer and one nitrate anion with the inversion center located on the Co ion. In complex **2**, the asymmetric unit contains one complete monomer and one tetraphenylborate anion. For complexes **1** and **2**, all non-hydrogen atoms are refined anisotropically and all H atoms are placed in calculated positions. Full crystallographic data for **1** and **2** are available upon request from the Cambridge Crystallographic Data Centre, 12 Union Road, Cambridge CB2 1EZ, U.K. (http://www.ccdc.cam.ac.uk/). The CCDC numbers are 925600 (**1**·123 K), 925601 (**1**·273 K), 925602 (**1**·353 K), and 925603 (**2**).

2.5. EPR Measurements. X-band (9.4−9.7 GHz) EPR spectra were recorded with a Bruker ESP380E CW/FT spectrometer. Sample temperatures from room temperature (293 K) to 110 K were obtained using the standard rectangular TE_{102} rectangular cavity, in conjunction with a Bruker VT 4111 temperature controller and its associated nitrogen gas flow insert. Spectra in the temperature range from 100 K down to 2.2 K were obtained using a Bruker ER4118 dielectric resonator inserted in an Oxford Instruments (Model CF 935 helium cryostat). Temperatures below 100 K were calibrated against a germanium thermometer, using a carbon resistor as a transfer standard. Microwave frequencies were measured with an EIP Microwave (Model 548A) frequency counter, and the g-factors were determined by reference to the F^+ line in CaO (g = 2.0001 ± 0.0001).[14] Spectral simulations were performed using the Bruker XSophe−Sophe-XeprView computer simulation software suite.[15]

2.6. DFT Calculations. The X-ray crystal structures of **1** were subject to DFT[16] calculations using the Gaussian 09 suite of programmes[17] to calculate the energetics of different spin configurations. Exchange coupling constant (J) values was calculated using the broken symmetry approach, as developed by Ginsberg and Noodleman.[18] The hybrid B3LYP[19] functional has been employed throughout our study. B3LYP has a proven track record of obtaining good numerical estimates of magnetic exchange in variety of transition metals, lanthanides, and metal-radical complexes.[20−22] However, there are also instances where B3LYP has failed to reproduce the correct ground state.[23] Here, we have employed the Ahlrichs triple-ζ valence (TZV)[24] basis set for all of the elements, as implemented in Gaussian 09. We have employed the following notation $^{mult}complex_{spin\ state}$ for our study to differentiate the different spin ground states arising from the exchange coupling and the spin state of the metal ions. Here, "mult" in the superscript denotes the total multiplicity of the computed state, while "spin state" in the subscript denotes the nature of the spin state (low-spin (LS) or high-spin (HS)) at the Co(II) center. The spin-density plots were generated using Molekel version 4.3 with a cutoff of 0.005, and MO diagrams are plotted using Chemcraft version 1.6.[25] Some selected low-lying spin configurations were also optimized using acetonitrile as a solvent and by employing the Polarizable Continuum Model (PCM).[26] Onsager's SCRF code extended by Wiberg and co-workers for Gaussian codes was applied to our system.[27,28] To calculate the magnetic susceptibility from the computed J values, we relied on the MAGPACK[29] software.

2.7. Electrochemistry. Voltammetric measurements were undertaken in acetonitrile (0.1 M $[Bu_4N](PF_6)$) at 293 ± 2 K under a flow of nitrogen gas or inside a glovebox using a BAS100B computer-controlled electrochemical workstation and a standard three-electrode cell. Glassy carbon (Cypress, 1-mm diameter for **1** and 1.5-mm diameter for **2**) macroelectrodes and a carbon fiber (7 μm diameter, ALS, Japan) microelectrode were used as the working electrode, whereas a platinum mesh and Ag/AgCl electrode was used as the counter and reference electrodes, respectively. The procedures employed for polishing the working electrode are described elsewhere.[30] All potentials given in this paper are referred to the ferrocene/ferrocenium ($[FeCp_2]^{0/+}$) reference couple. Mechanistic aspects of the voltammetric processes were investigated by applying the appropriate diagnostic criteria.[31]

dx.doi.org/10.1021/ic400565h | Inorg. Chem. 2013, 52, 7557−7572

3. RESULTS AND DISCUSSION

3.1. Synthesis and Structure. $[Co^{II}(L^{\bullet})_2](NO_3)_2$ (**1**) was isolated by reacting 4,4-dimethyl-2,2-di(2-pyridyl) oxazolidine *N*-oxide ($L^{\bullet}$) with $[Co^{II}(NO_3)_2]\cdot 6H_2O$ in a 2:1 ratio in MeCN. Diffusions of Et_2O into the resultant brown solution produced crystalline **1** in ∼30% yield. Complex **2** was isolated by reacting $L^{\bullet}$ with $Co^{II}SO_4\cdot 7H_2O$ and $NaBPh_4$ in MeOH in a 2:1:2 ratio, and the resulting brown precipitate was dissolved in dichloromethane (DCM), followed by Et_2O diffusion to yield crystalline **2** in ∼40% yield. A small number of crystals of **2** could be obtained by Et_2O diffusions of the MeOH filtrate. Complexes **1**·123 K, **1**·273 K, **1**·353 K, and **2** crystallize in the monoclinic space group $P2_1/c$, with the asymmetric unit of **1** containing half the $[Co^{II}(L^{\bullet})_2]^{2+}$ dication and one nitrate anion, while **2** contains one complete $[Co^{III}(L^{-})_2]^{+}$ monocation and one tetraphenylborate anion (see Figures 2 and 3). An inversion center sits on the cobalt in **1** generating the $[Co^{II}(L^{\bullet})_2]^{2+}$ dication. Both the dication $[Co^{II}(L^{\bullet})_2]^{2+}$ and monocation $[Co^{III}(L^{-})_2]^{+}$ are structurally similar but vary in a few significant bond lengths and angles, which, along with electrochemistry, EPR, and magnetic studies (vide infra), help us to assign oxidation and spin states of the central Co ion, as well as assignment of the neutral radical ($L^{\bullet}$) or anionic form (L^{-}) of the ligand.

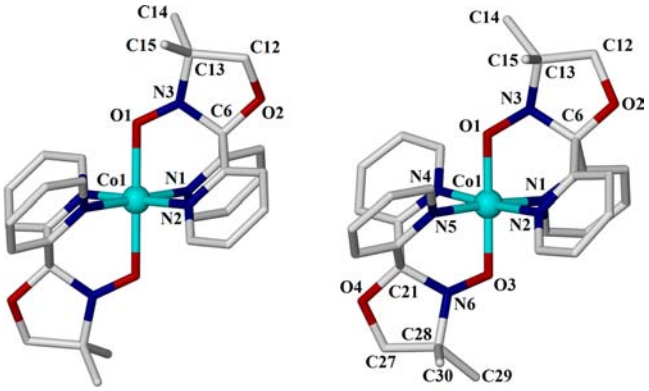

Figure 2. Molecular structure of the dication $[Co^{II}(L^{\bullet})_2]^{2+}$ in **1**·123 K (left) and the monocation $[Co^{III}(L^{-})_2]^{+}$ in **2** (right). The structure and atomic labeling in **1**·123 K is representative of **1**·273 K and **1**·353 K. Hydrogen atoms and anions omitted for clarity. Legend: oxygen, red; nitrogen, dark blue; and cobalt, turquoise.

Each tridentate ligand coordinates to the Co ion equatorially via two pyridyl donors and axially via the oxygen, completing the coordination sphere (see Figure 2). In **1**·123 K, this results in an axially elongated octahedral geometry (cis, 86.99(13)°−93.01(13)°; trans, all 180°; Co−O 2.113(3)Å, Co−N 1.959(3), 1.986(3)Å). Upon heating complex **1** we see a trend toward a more perfectly realized octahedral geometry (see Figure 3 and Table 2) with a marked increase in the Co−N bond lengths and an accompanying small decrease in the Co−O bond length (**1**·273 K: cis, 85.44(8)°−94.56(8)°; trans, all 180°; Co−O, 2.117(2) Å; Co−N, 2.040(2), 2.056(2) Å; **1**·353K, 84.77(14)°−95.23(14)°; trans, all 180°; Co−O, 2.107(3) Å; Co−N, 2.056(3), 2.073(4) Å). In **2**, there is a slight axial compression (cis, 85.86(11)°−97.81(11)°; trans, 170.62(10)°−175.91(12)°; Co−O, 1.879(2), 1.892(2) Å; Co−N, 1.916(3), 1.921(3), 1.928(3), 1.930(3) Å) (see Figure S1 in the Supporting Information and Table 3). The nitroxide N−O bond lengths are 1.294(4) Å in **1** and 1.401(3) and 1.411(3) Å in **2**. To accommodate the longer nitroxide N−O bond lengths in **2** the five membered ring of the ligand is buckled quite significantly (Figure S2 in the Supporting Information). In **1**,

Table 2. Selected Bond Lengths and Angles for 1·123 K, 1·273 K, and 1·353 K

	$[Co^{II}(L^{\bullet})_2]^{2+}$		
	1·123 K	**1**·273 K	**1**·353 K
Bond Lengths (Å)			
Co(1)−O(1)	2.113(3)	2.117(2)	2.107(3)
Co(1)−N(1)	1.959(3)	2.040(2)	2.056(3)
Co(1)−N(2)	1.986(3)	2.056(2)	2.073(4)
O(1)−N(3)	1.294(4)	1.285(2)	1.285(4)
N(3)−C(6)	1.455(5)	1.478(3)	1.481(6)
N(3)−C(13)	1.478(5)	1.480(3)	1.471(5)
C(6)−O(2)	1.416(5)	1.397(3)	1.394(5)
O(2)−C(12)	1.429(6)	1.387(4)	1.369(6)
C(12)−C(13)	1.547(7)	1.510(4)	1.494(8)
C(13)−C(14)	1.515(6)	1.509(4)	1.504(8)
C(13)−C(15)	1.505(6)	1.499(4)	1.496(7)
Bond Angles (deg)			
Co(1)−O(1)−N(3)	115.4(2)	115.13(13)	115.5(2)

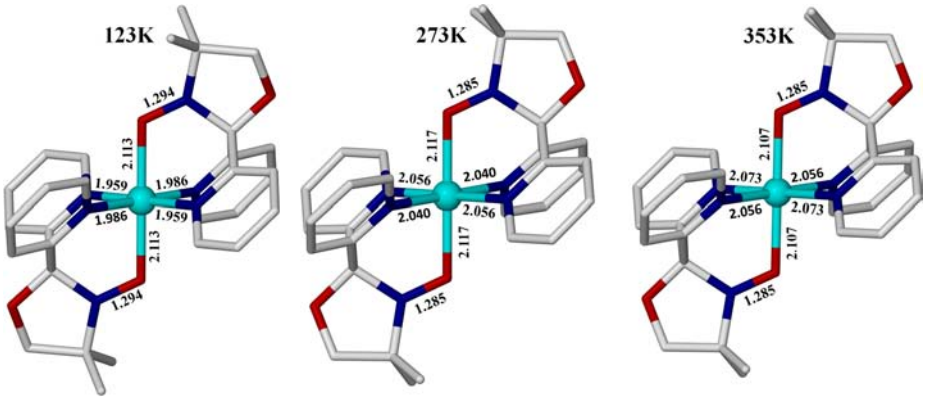

Figure 3. Molecular structure of the dication $[Co^{II}(L^{\bullet})_2]^{2+}$ in **1**·123 K (left), **1**·273 K (middle), and **1**·353 K (right), with relevant bond lengths given in Ångstroms without uncertainties (see Table 2). Hydrogen atoms and anions are omitted for clarity. Legend: oxygen, red; nitrogen, dark blue; and cobalt, turquoise.

dx.doi.org/10.1021/ic400565h | Inorg. Chem. 2013, 52, 7557−7572

Table 3. Selected Bond Lengths and Angles for 2 at 123 K

	2, $[Co^{III}(L^{-})_2]^+$
Bond Lengths (Å)	
Co(1)−O(1)	1.879(2)
Co(1)−O(3)	1.892(2)
Co(1)−N(1)	1.930(3)
Co(1)−N(2)	1.928(3)
Co(1)−N(4)	1.921(3)
Co(1)−N(5)	1.916(3)
O(1)−N(3)	1.411(3)
O(3)−N(6)	1.401(3)
N(3)−C(6)	1.483(4)
N(3)−C(13)	1.487(4)
C(6)−O(2)	1.403(4)
O(2)−C(12)	1.444(4)
C(12)−C(13)	1.519(5)
C(13)−C(14)	1.512(5)
C(13)−C(15)	1.526(4)
N(6)−C(21)	1.472(5)
N(6)−C(28)	1.491(5)
C(21)−O(4)	1.407(4)
O(4)−C(27)	1.448(4)
C(27)−C(28)	1.501(5)
C(28)−C(29)	1.530(5)
C(28)−C(30)	1.515(5)
Bond Angles (deg)	
Co(1)−O(1)−N(3)	111.73(18)
Co(1)−O(3)−N(6)	111.80(19)

two nitrate anions are present per dication with no significant intermolecular interactions or lattice solvent present and the shortest distance (O_{NO}−O_{NO}) between neighboring nitroxide N−O groups is 6.586 Å. In **2**, one tetraphenylborate anion is present per cation with, again, no significant intermolecular interactions or lattice solvent present.

The pseudo-Jahn−Teller distortion in **1**·123 K contrasts with the Fe−O distances of 1.876(2) and 1.884(2) Å and the Fe−N distances in the range of 1.962(2)−1.989(2) Å found in the analogous low-spin $[Fe^{II}(L^{\bullet})](BF_4)_2$ complex[12] and suggests we have a typical low-spin d^7 Co ion at 123 K, where the unpaired electron lies in the σ-antibonding orbital d_{z^2}. Higher-temperature structures at 273 K (**1**·273 K) and 353 K (**1**·353 K) reveal the gradual disappearance of this pseudo-Jahn−Teller distortion, such that **1**·353 K has a final Co−O bond length of 2.107(3) Å and Co−N bond lengths of 2.056(3) Å and 2.073(4) Å (see Figure 3, Table 2). The pseudo-Jahn−Teller distortion at 123 K is evidenced by the shortening of the four equatorial Co−N bond lengths (see Figure 3 and Table 2), which then lengthen as we increase the temperature. The Co−O bond length is unaffected by an increase in temperature, with the three Co−O bond lengths (2.113(3) Å at 123 K, 2.117(2) Å at 273 K, and 2.107(3) Å at 353 K) remaining effectively the same when we consider the standard deviations. Libration effects[32] in high-temperature structural studies leads to bond-length shortening, which confirms that the overall increase in bond length seen here represents a significant change in the electronic structure of complex **1**. A strong pseudo-Jahn−Teller effect is expected for the low-spin $2E(t_{2g}^6e_g^1)$ state, in comparison to the high-spin $^4T_1(^{t}_{2g}{}^5e_g^2)$ state for Co(II), which leads us to propose that the disappearance of such a distortion as we increase the temperature is consistent with a gradual spin crossover. The average bond length difference around the octahedral Co(II) ion at 123 and 353 K is 0.0424 Å, which is lower than the range of 0.07−0.11 Å observed for complete Co(II) spin crossover,[33] suggesting that the spin transition is incomplete at 353 K. This is confirmed by magnetic susceptibility measurements (vide infra) made up to 400 K.

The overall bond-length shortening and large reduction on Co−O bond lengths in particular in **2** is consistent with a diamagnetic low-spin Co^{3+} center, where the greater charge density and unfilled antibonding e_g orbital set contributes to the short distances, as seen previously in the analogous low-spin complex $[Fe^{III}(L^{-})_2](BPh_4)\cdot 0.5H_2O$[12] (see Figure S1 in the Supporting Information and Table 3).

Nitroxide N−O bond lengths are useful in assigning the ligand to the neutral radical ($L^{\bullet}$) or anionic hydroxylamino form (L^{-}). For the conceptually similar ligands Tempo and Proxyl, typical free ligand nitroxide radical N−O bond lengths lie between 1.27 and 1.28 Å,[6c] coordinated nitroxide radical N−O bond lengths lie in the range of 1.261(12)−1.300(3) Å[34−40] and coordinated hydroxylamino anion or hydroxylamine groups

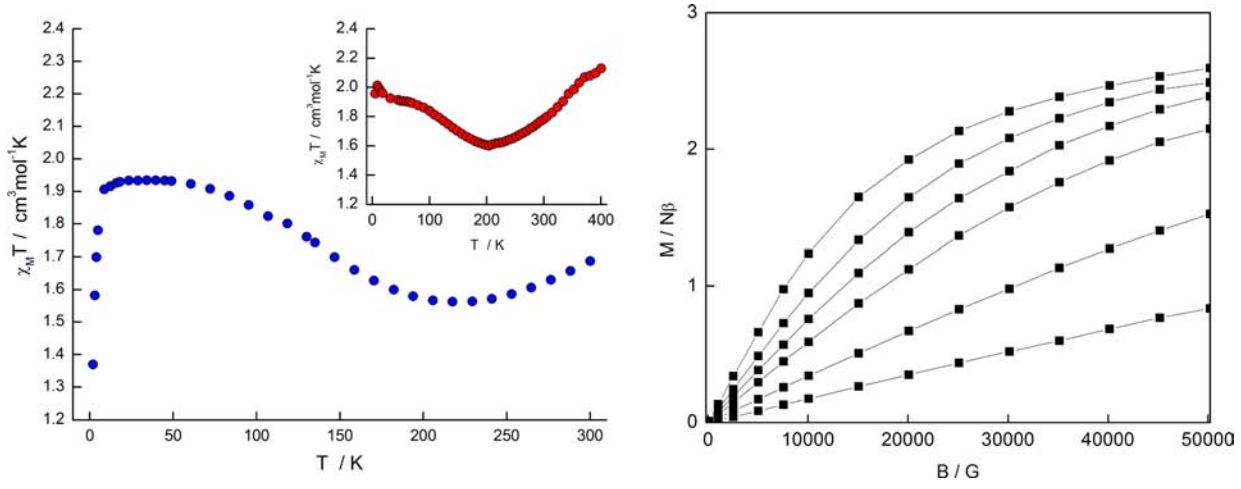

Figure 4. (Left) Plot of $\chi_M T$ vs T for **1** between 2 K and 300 K in (black circles) and between 5 K and 400 K (red circles, inset) in an applied field of 10 000 G. (Right) Plot of M ($N\beta$) vs field (0−50 000 G) at 2 K (top), 3 K, 4 K, 5.5 K, 10 K, and 20 K (bottom). The black solid lines are a guide only.

dx.doi.org/10.1021/ic400565h | Inorg. Chem. 2013, 52, 7557−7572

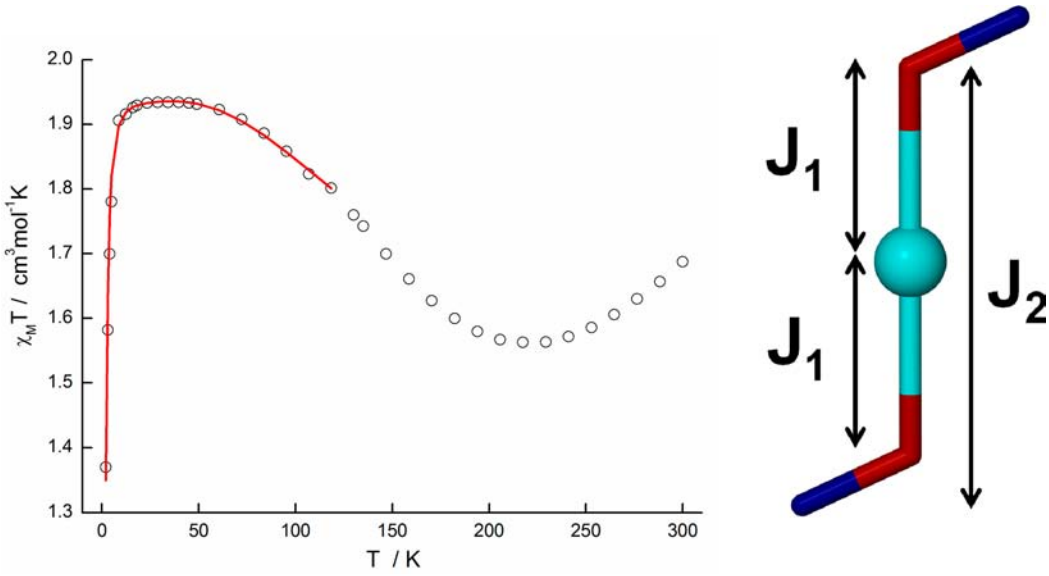

Figure 5. Plot of $\chi_M T$ vs T for **1** in the temperature range of 2−300 K (left). The solid red line represents a fit of the experimental data in the temperature range of 2−119 K to an exchange interaction model shown (right).

have N−O bond lengths in the range of 1.379(5)−1.413(3) Å.[41−43] The N−O bond lengths of 1.294(4) Å in **1** suggests both ligands in **1** are in the neutral radical form ($L^{\bullet}$), whereas the longer N−O bond lengths found in **2** of 1.401(3) Å and 1.411(3) Å suggest both ligands are in the anionic hydroxylamino form (L^{-}). The assignments of a Co(II) gradual spin-crossover with two neutral radical ligands ($L^{\bullet}$) in **1** ($[Co^{II}(L^{\bullet})_2](NO_3)_2$) and a low-spin d^6 Co(III) ion with two anionic hydroxylamino ligands (L^{-}) in **2** ($[Co^{III}(L^{-})_2](BPh_4)$) have been made, not only on the basis of crystallographic data but also from interpretation of magnetic measurements, electrochemistry, EPR, and DFT calculations (vide infra).

3.2. Magnetic Studies. Direct current (DC) magnetic susceptibility measurements were performed on a bulk sample of crystals of $[Co^{II}(L^{\bullet})_2](NO_3)_2$ (**1**) in the 300-2 K range under an applied field of 10 000 G (Figure 4, left). Magnetization measurements on **1** were undertaken between 2 K and 20 K in the applied field range of 0−50 000 G (Figure 4, right). Both the 2−300 K magnetic susceptibility and the magnetization measurements were performed on crystalline complex **1** in a petroleum jelly mull to minimize any torquing effects. A second susceptibility measurement was performed between 5 K and 400 K under an applied field of 10 000 G (Figure 4, left, inset) with polycrystalline sample **1** unrestrained, in a quartz tube, to confirm the apparent increase in the $\chi_M T$ value as T is increased from ∼225 K. The two susceptibility measurements have similar, but not identical, profiles, with the only significant deviation being at lower temperatures where the 5−400 K measurement shows a small maximum at 8.7 K, possibly attributable to torquing effects. Alternating current (AC) magnetic susceptibility measurements were performed on crystalline complex **1** between 2 and 20 K, in applied DC fields of 0, 2000, and 5000 G and oscillating frequencies in the range 50−1500 Hz. Direct current (DC) magnetic susceptibility measurements were also performed on crystals of $[Co^{III}(L^{\bullet})_2](BPh_4)$ (**2**) and show that the compound is diamagnetic, as expected.

For complex **1** measured between 2 K and 300 K, the $\chi_M T$ value of 1.69 $cm^3\ mol^{-1}$ K at 300 K decreases slowly upon cooling to a $\chi_M T$ value of 1.56 $cm^3\ mol^{-1}$ K at 218 K, which then increases rapidly to a broad maximum starting at 40 K with a $\chi_M T$ value of 1.93 $cm^3\ mol^{-1}$ K (Figure 4, left) The $\chi_M T$ value then decreases rapidly upon further cooling, most likely because of a combination of Zeeman and zero-field splitting effects, reaching a final value of 1.37 $cm^3\ mol^{-1}$ K at 2 K. The maximum $\chi_M T$ value of 1.93 $cm^3\ mol^{-1}$ K at 40 K is slightly higher than the expected $\chi_M T$ value for a $S = {}^3/_2$ ground state (assuming g = 2.00) of 1.875 $cm^3\ mol^{-1}$ K. This behavior is indicative of ferromagnetic exchange between the $S = {}^1/_2$ centers on the radical ligands and the low-spin Co(II) $S = {}^1/_2$, resulting in a $S = {}^3/_2$ ground state.

The $\chi_M T$ vs T data in the temperature range of 2−119 K could be fitted satisfactorily with program PHI,[44] using a 2J trimer model (Figure 5) with the spin Hamiltonian $\hat{H} = -2J_1(\hat{S}_1\cdot\hat{S}_2 + \hat{S}_2\cdot\hat{S}_3) - 2J_2(\hat{S}_1\cdot\hat{S}_3)$ where J_1 describes the interaction between the radicals (S_1 and S_3) and the Co(II) ion (S_2) and J_2 the radical−radical interaction via the low-spin Co(II) ion. The best-fit parameters are as follows: J_1 = +63.8 cm^{-1}, J_2 = +63.9 cm^{-1}, and g = 2.10.

Since the electron spins are coupled ferromagnetically, a quartet state lies lowest at energy $-J_1 - J_2/2$, and there are doublet states at ${}^3/_2 J_2$ and $2J_1 - J_2/2$.[45] This results in a well-isolated $S = {}^3/_2$ ground state with the two excited state $S = {}^1/_2$ doublets 191.4 cm^{-1} ($3J_1$) and 191.6 cm^{-1} ($J_1 + 2J_2$) higher in energy. The $\chi_M T$ vs T data could also be fitted from 2 K to 205 K (see Figure S3 in the Supporting Information), yielding the parameters J_1 = +58.0 cm^{-1}, J_2 = +58.8 cm^{-1} and g = 2.10, also giving an $S = {}^3/_2$ ground state, although the fits were of lesser quality. The excellent fit to the $\chi_M T$ vs T data (see Figure 7, presented later in this paper) below 119 K strongly suggests that the majority of the Co(II) ions are in the LS state below this temperature, while the lower-quality higher-temperature $\chi_M T$ vs T fit (see Figure S3 in the Supporting Information) suggest an increasing population of HS Co(II) ions. These fits do not take into account the contributions to the magnetic susceptibility from the introduction of the spin crossover of the Co(II) ion and possible antiferromagnetic exchange (vide infra) between the emerging high-spin Co(II) ions and the radicals, which becomes more prevalent at higher temperatures. The radical−radical exchange interaction via the low-spin Co(II) ion

dx.doi.org/10.1021/ic400565h | Inorg. Chem. 2013, 52, 7557−7572

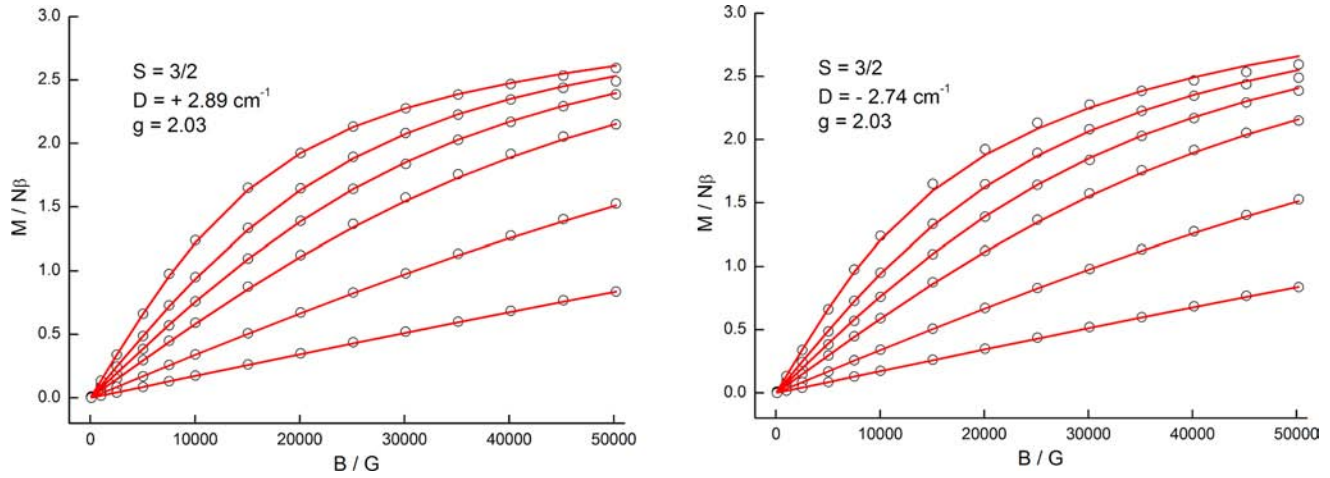

Figure 6. Plot of M ($N\beta$) vs field (0 − 50,000 G) at (top), 3, 4, 5.5, 10, and 20 K (bottom). The solid red lines represent fits of the experimental data with the parameters shown and in the text, D being positive (left) and negative (right).

is of a similar magnitude to the radical-Co(II) ion interaction (~60 cm^{-1}), which seems counterintuitive, but we have previously reported a large radical−radical (J_2) antiferromagnetic exchange (J = −315 cm^{-1} using the spin Hamiltonian $-2J(\hat{S}_1\cdot\hat{S}_2)$ via the low-spin Fe(II) ion in the analogous compound $[Fe^{II}(L^{\bullet})_2](BF_4)_2$.[12] The magnitude and type of exchange between the radical and metal ion is highly dependent on geometrical parameters, which affects the degree of overlap between the metal and ligand-based orbital(s). The interaction between the radical π^* orbital and the Co(II) magnetic orbital, which is expected to be mainly d_{z^2} in character, in this case, is ferromagnetic, which suggests that they are orthogonal in nature. This fit treats the low-spin Co^{II} as an isotropic $S = {}^1/_2$ with a g-value of >2, because of close lying excited states. The possibility of a small residual fraction of the high-spin Co(II) dication and admixture of closely lying excited states into the ground state are not explicitly accounted for in the model. Indeed the M vs H data (Figure 4) do not saturate to the expected M value of 3 $N\beta$ for an isolated $S = {}^3/_2$ ground state, even at 2 K in an applied field of 50 000 G. The M vs H data could be fitted satisfactorily with PHI,[44] using the giant spin approximation with $S = {}^3/_2$ (see Figure 6) yielding the parameters g = 2.03 and D = +2.89 cm^{-1}. The corresponding Hamiltonian is given by eq 1:

$$\hat{H} = DS_z^2 + E(S_x^2 - S_y^2) + g\mu_B\vec{B}\cdot\vec{S} \quad (1)$$

where D is the axial anisotropy, μ_B the Bohr magneton, S_{z^2} the easy-axis spin operator, and B the applied field. However, these data could also be fitted with a negative D value, yielding the parameters g = 2.03 and D = −2.74 cm^{-1}. The combination of the susceptibility and magnetization fits give us a consistent view of an $S = {}^3/_2$ system with a g-value greater than the free-electron value and a nonzero axial zero-field splitting parameter D. The assignment of an $S = {}^3/_2$ ground state and nonzero D value is confirmed by EPR measurements (vide infra), which suggest we also have a nonzero E (rhombic zero-field splitting) parameter that allows mixing of the pure m_S states within the $S = {}^3/_2$ manifold.

AC susceptibility data were obtained on **1** with measurements undertaken between 1.8 K and 20 K in zero DC field with a 3.5 G AC field oscillating with frequencies ranging from 50 Hz to 1500 Hz. In zero field, the imaginary component of the susceptibility χ''_M is negligible and close to zero, leading us to examine the effect on the χ''_M values and their frequency dependence with static DC field variations. These measurements were undertaken at 2 K in a 3.5 G AC field oscillating with frequencies ranging from 1 Hz to 1500 Hz in applied static DC fields of 2000−15 000 G. At 2000 G, the χ''_M value reached a maximum of 0.22 cm^3 mol^{-1} at 1500 Hz and 2 K, while at 5000 G, the χ''_M value peaks around a maximum of 0.18 cm^3 mol^{-1} at 1400 Hz and 2 K with an obvious downturn at higher frequencies. To investigate this further, AC susceptibility measurements were undertaken under static DC fields of 2000 and 5000 G and plotted as χ''_M vs T (Figure 7). Upon cooling, the imaginary component of the susceptibility χ''_M shows some frequency dependence, finally reaching a value of 0.24 cm^3 mol^{-1} at 1500 Hz and 1.8 K in 2000 G. In a 5000 G static DC field, we observe a peak maxima centered at 2 K and 1500 Hz with a χ''_M value of 0.17 cm^3 mol^{-1}. To investigate this possible SMM-like behavior, we plotted ln (χ''_M/χ'_M) vs $1/T$ for **1** at differing frequencies, and applying linear fits, we have estimated E_a ≈ 10.6 K and $\tau^\circ \approx 10^{-6}$ s at 2000 G and E_a ≈ 7.6 K and $\tau^\circ \approx 10^{-6}$ s in 5000 G (see Figure S5 in the Supporting Information). The appearance of such temperature- and frequency-dependent peaks in the AC susceptibility measurements under an applied DC field suggests a negative D-value whose magnitude is at least 3.7 cm^{-1}, when considering the relationship concerning the upper limit of the energy barrier for half-integer spins $U = (S^2 - {}^1/_4)|D|$ and is consistent with the magnitude of ~2.7 cm^{-1} for D found in the fits of M ($N\beta$) vs field (see Figure 6). Although we cannot unambiguously determine the sign of D from fits to the M vs H data, we were unable to simulate the EPR spectrum at 2.2 K (see Figure 9, presented later in this work) with D < 0, the simulations yielding positive D and nonzero E values.

Similar field-induced slow magnetic relaxation effects in materials with positive D values were observed in the octahedral mononuclear Co(II) complex, *cis*-$[Co^{II}(dmphen)_2(NCS_2)]\cdot 0.25EtOH$, where dmphen = 2,9-dimethyl-1,10-phenanthroline, and these were due to a transverse anisotropy barrier governed by the E parameter.[46a] In this case, it may be expected that, for the $M_s = \pm{}^1/_2$, Kramers doublet ground-state quantum tunneling effects would prevent such a preferential axis in the xy-plane; however, upon applying a DC field, these effects are quenched. In that work,[46a] the reported energy barrier for the relaxation of the magnetization ΔE = 16.2−18.1

dx.doi.org/10.1021/ic400565h | Inorg. Chem. 2013, 52, 7557−7572

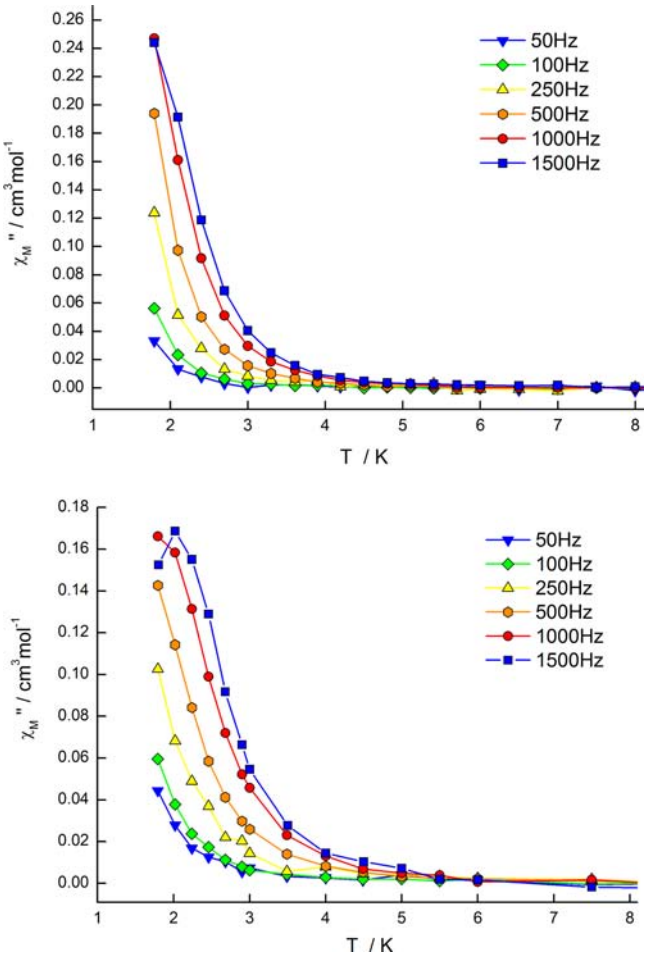

Figure 7. Plot of χ_M'' vs T for complex **1** in an applied DC field of 2000 G (top) and 5000 G (bottom) at frequencies shown.

cm^{-1} matched the theoretical transverse barrier for rotation in the xy plane of $\Delta E = 2E = 16.8\ cm^{-1}$ given the reported experimental E value of 8.4 cm^{-1}. In addition, a high-field EPR spectroscopic study on model compounds based on the single-chain magnet (SCM) $(DMF)_4MnReCl_4(CN)_2$[46b] found that the slow magnetic relaxation effects in $(DMF)_4MnReCl_4(CN)_2$ were due to the transverse E term associated with the Re^{IV} ion, where the quantum tunneling effects were suppressed, in that case, by the intrachain spin correlations. In both cases mentioned above, slow magnetic relaxation effects were observed with the presence of an easy-plane anisotropy ($D > 0$) and a significant E component. However, in a pseudo-tetrahedral Co(II) complex $[(3G)CoCl](CF_3SO_3)$,[46d] where 3G = 1,1,1-tris[2*N*-(1,1,3,3-tetramethylguanidino)methyl]-ethane, AC data showed field-induced slow magnetic relaxation with positive D and E values; however, in this case, it was suggested that the relaxation mechanism followed an Orbach pathway through the excited state $M_s = \pm^3/_2$ levels after a field-induced bottleneck of the direct relaxation between the ground $M_s = \pm^1/_2$ states. This was rationalized by consideration of the experimental energy barrier for the relaxation of the magnetization $\Delta E = 24\ cm^{-1}$, which closely matched the separation between the $M_s = \pm^1/_2$ and $M_s = \pm^3/_2$ states and not the theoretical transverse barrier. A similar Orbach mechanism was also reported for the trinuclear Cu(II) complex $[Bu_4N_2][Cu_3(\mu\text{-}Cl)_2(\mu\text{-}pz)_3Cl_3]$,[46e] where pz = the pyrazolato anion, which showed slow magnetic relaxation effects under applied fields. Additional compounds which showed slow magnetic relaxation effects with $D > 0$ include the mixed-valence SCM $[Fe^{II}(ClO_4)_2\{Fe^{III}(bpca)_2\}]ClO_4$ where Hbpca = bis(2-pyridylcarbonyl)amine[46f] and the heterometallic complex $[Fe_3Cr(L)_2(dpm)_6]\cdot Et_2O$,[46g] where H_3L = 2-hydroxymethyl-2-phenylpropane-1,3-diol and Hdpm = dipivaloylmethane.

It may be expected, then, that if the experimentally derived energy barrier for the relaxation of the magnetization for complex **1** is similar to the transverse anisotropy barrier of $\Delta E = 2E$, this would suggest that the relaxation mechanism involves a transverse anisotropy barrier; however, if it is similar to the energy gap between the $M_s = \pm^1/_2$ and $M_s = \pm^3/_2$ states, this would imply that the relaxation mechanism follows an Orbach pathway. Unfortunately, we have no direct experimentally derived values for the energy barrier for the relaxation of the magnetization due to the absence of discernible peaks in the χ''_M vs T plots (the reported values previously are estimations only (see Figure S5 in the Supporting Information)). Therefore, we cannot compare the experimental energy barrier for the relaxation of the magnetization with the theoretical transverse anisotropy barrier or indeed the energy gap between the $M_s = \pm^1/_2$ and $M_s = \pm^3/_2$ states, so we cannot comment, with any degree of confidence, on the exact nature of the relaxation mechanism in complex **1**.

The radical-based complex $[Co(hfpip)_2(4NOpy)_2]$ in the diluted frozen solution reported by Koga et al.[46c] is a $S = {}^3/_2$ SMM with a U_{eff} value of ∼29 K and highlights the potential that even monometallic radical species, such as those reported here, have in this regard.

The previous DC susceptibility fits are based on the low-temperature magnetic data; however, as we increase the temperature, we see an increase in the $\chi_M T$ value of 1.56 $cm^3\ mol^{-1}\ K$ at 218 K to a value of 1.69 $cm^3\ mol^{-1}\ K$ at 300 K (see Figure 4). A second measurement undertaken between 5 K and 400 K (Figure 4, inset) confirms this increase in the $\chi_M T$ values, finally reaching a value of 2.13 $cm^3\ mol^{-1}\ K$ at 400 K, which suggests the possibility of the Co(II) center undergoing a gradual spin-crossover transition. In cobalt(II) spin-crossover d^7 systems, only one electron is transferred to the antibonding e_g orbital set, which results in a smaller average bond length change of ∼0.10 Å, compared to ∼0.20 Å seen in typical Fe(II) d^6 spin transitions. In addition, the majority of the spin-transition curves for Co(II) compounds are of a gradual nature and complementary techniques such as Mössbauer spectroscopy, used for Fe(II), are unavailable for Co(II) systems. In the next section, we see that EPR spectroscopy is useful in identifying the doublet state ($^{2E}(t_{2g}^6e_g^1)$) of low-spin Co(II) giving valuable information on the local symmetry, anisotropy, and splitting of the ground state. Spin−lattice relaxation effects broaden the resonances from high-spin Co(II) to such an extent that they are usually only observable at very low temperatures. Temperature-dependent magnetic susceptibility, however, remains the main technique for studying Co(II) spin crossover, but even this remains difficult with ligand-field strength, spin−orbit coupling effects, and doublet and quartet levels mixing in the spin-crossover region making an unambiguous magnetic analysis very difficult.[47] For example, the 400 K $\chi_M T$ value of 2.13 $cm^3\ mol^{-1}\ K$ in complex **1** could represent anywhere between a 60% and 80% incomplete gradual spin crossover. Fortunately, in this case, the low-spin octahedral Co(II) ion exhibits a strong pseudo-Jahn−Teller distortion, which we have monitored by means of variable-temperature crystallographic measurements (see Figure 3,

dx.doi.org/10.1021/ic400565h | Inorg. Chem. 2013, 52, 7557−7572

Table 2). At 123 K, we have an unambiguous low-spin Co(II) ion, exhibiting a pseudo-Jahn−Teller distortion, which disappears with an increase in temperature up to 353 K. The disappearance of this distortion suggests complex **1** undergoes an incomplete, gradual spin transition up to 400 K, which is consistent with the magnetic susceptibility measurements. In summary, compound **1** is a rare, perhaps unique, example of a mixed radical−d-block complex displaying magnetic exchange, spin-crossover features, and slow magnetic relaxation (SMM) effects.

3.3. EPR Spectroscopy of $[Co^{II}(L^{\bullet})_2](NO_3)_2$ (1). At 295 K, the spectrum of **1** over the field range from 50 G to 6000 G only exhibited an intense symmetric resonance of width ∼80 G and centered on $g \approx 2.003$, as shown in Figure 8. The spectrum remained unchanged until the temperature was reduced to ∼120 K, when a broad but rather less-intense resonance could be discerned at $g \approx 3.7$, which extended from 1200 G to above ∼2200 G. Although the $g \approx 2$ resonance had a similar peak-to-peak derivative width at 110 K, since, at 295 K, there appeared to be rather more intensity in the wings at the lower temperature (Figure 8). As shown in Figure 8, further reductions in temperature resulted in a narrowing and an increase in the intensity of the feature at $g \approx 3.7$, relative to that at $g \approx 2$, and a rather less-symmetric appearance of the latter. At temperatures below ∼20 K, the $g \approx 3.7$ resonance was of similar intensity to the $g \approx 2$ resonance and began to show a resolved feature on the low-field side at with a peak at ∼1550 G. The shoulder feature on the $g \approx 3.7$ resonance and the change in shape of that at $g \approx 2.0$ are most clearly seen at 2.2 K, as shown in Figure 8. It can also be seen that, as well as becoming less symmetric, the $g \approx 2$ resonance had broadened to a width of ∼150 G and shifted to a g-value of 1.99.

The fit of the 2.2 K spectrum was approached using the SOPHE program[15] and two different models, as shown in Figure 9. The first, shown in Figure 9a, assumed that the

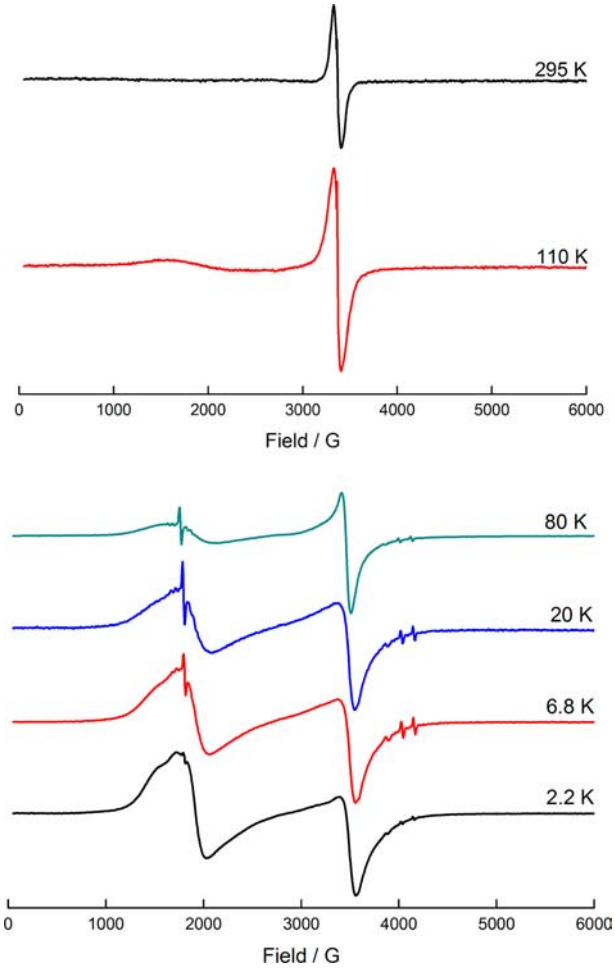

Figure 8. EPR spectra of polycrystalline **1** at the temperatures indicated. Spectrometer settings: upper spectra (295 and 110 K), microwave frequency = 9.434 GHz; microwave power = 5.26 mW; receiver gain = 1.0×10^5; 100 kHz modulation amplitude = 0.2 mT; field scan range/time = 600 mT/84 s; time constant = 41 ms. Lower spectra (80 K, 20 K, 6.8 K, 2.2 K): microwave frequencies = 9.704 GHz (80 K, 20 K, 6.8 K), 9.691 GHz (2.2 K); microwave power = 1.05 mW (80 K), 10.5 μW (20 K, 6.8 K, 2.2 K); receiver gain = 1.0×10^4 (80 K), 1.0×10^5 (20 K), 2.5×10^4 (6.8 K, 2.2 K); 100 kHz modulation amplitude = 0.1 mT; field scan range/time = 600 mT/84 s; time constant = 41 ms.

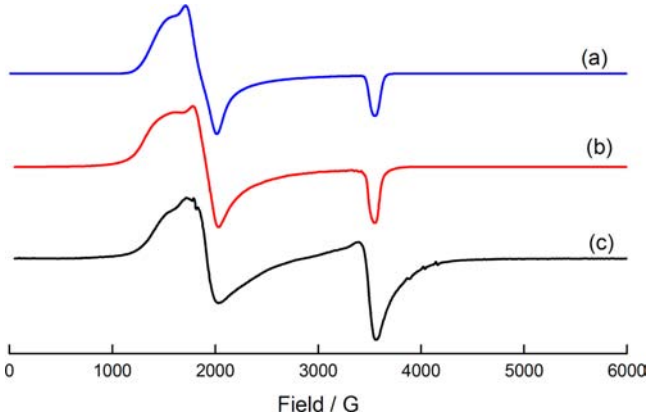

Figure 9. Comparison of simulated spectra (a, b) as described in the text with experimental spectrum (c) of **1** recorded at 2.2 K (see Figure 10). The spin Hamiltonian and linewidth parameters for the simulated spectrum are listed in Table 4. Spectrum (a) is for "high spin Co (II)" Sz = $\pm^1/_2$ doublet and Gaussian line shape; spectrum (b) is for SOPHE with $S = {}^3/_2$ and Lorentzian line shape.

resonances were due to $M_s = \pm 1$ transitions within a Kramers doublet with effective spin $S = {}^1/_2$. The second assumed a system with spin $S = {}^3/_2$, where the zero-field splitting parameters D and E were two of the variables (Figure 9b). The parameters giving the best fits to the experimental spectrum are listed in Table 4.

We note that the narrow resonances at ∼1750 G and 4000 G are due to cavity artifacts and the "hump" at ∼3400 G is most likely due to a radical impurity.

The simulation of Figure 9a, assuming a spin $S = {}^1/_2$, and gave effective g-values of $g_x = 4.50$, $g_y = 3.71$, and $g_z = 1.955$, which are clearly not appropriate for $S = {}^1/_2$ for either a radical or for low-spin Co(II). They are also not consistent with expectation for transitions within the low-lying $M_S = \pm {}^1/_2$ Kramers doublet of high-spin Co(II), for the following reasons:

(i) the average g-value here is ∼3.3, whereas, for most Co(II) high-spin systems, it is ∼4.3,[48] and

(ii) the hyperfine interactions obtained through the simulation appear to be rather too small for a high-spin Co(II) system.[49]

We also note here that a zero-field splitting of ≥50 cm^{-1} is considered appropriate for six-coordinated high spin Co(II),

dx.doi.org/10.1021/ic400565h | Inorg. Chem. 2013, 52, 7557−7572

Table 4. Spin Hamiltonian and Linewidth Parameters Used To Simulate the Spectra Shown in Figure 9[a]

	"$S = {}^1/_2$"	SOPHE,[15] $S = {}^3/_2$
g_x	4.50	2.090
g_y	3.71	2.050
g_z	1.955	1.990
A_x	80	45
A_y	60	25
A_z	12	12
D		7.0
E/D	0.064	0.075
σ_x	60	20
σ_y	50	20
σ_z	25	20
$\delta g_x/g_x$	0.08	−0.08
$\delta g_y/g_y$	0.02	0.025
$\delta g_z/g_z$	0	0

[a]Hyperfine parameters, and linewidths are in units of 10^{-4} cm^{-1}, while the zero-field splitting parameter D is in cm^{-1}. Uncertainties for the $S = {}^3/_2$ SOPHE simulation spin Hamiltonian parameters are estimated as follows: g-values, ±0.005; A-values ($\times 10^{-4}$ cm^{-1}) A_x, A_y ± 5, A_z ± 2; D ± 1.0 cm^{-1}; E/D ± 0.005. The ratio E/D for the "$S = {}^1/_2$" case was calculated using the g-values listed here and the equations of Pilbrow.[54]

and this is rather larger than that found here (vide infra).[50] The most viable interpretation of the EPR spectrum at 2.2 K is that suggested by a consideration of the X-ray crystallographic and magnetic susceptibility measurements, namely, that it arises from an approximately linear trimeric spin system composed of a low-spin ($S = {}^1/_2$) Co(II) ion bracketed by two radicals, each with spin $S = {}^1/_2$. As described above, for the present linear trimeric system, where J_1 and J_2 are both strong and ferromagnetic (J_1 = 63.8 cm^{-1} and J_2 = 63.9 cm^{-1}), a quartet state ($S = {}^3/_2$) lies lowest in energy and is well-isolated from the two $S = {}^1/_2$ doublets, which lie $3J_1$ and $J_1 + 2J_2$ higher in energy, relative to the ground state. Thus, the resonances observed at 2.2 K arise from transitions within the quartet state, and the simulations shown in Figure 9b, proceed on this basis, giving the parameters listed in Table 4. In order to arrive at the simulated spectrum shown in Figure 9b using SOPHE, it was necessary to assume that the x- and y-axes of the zero-field splitting tensor were interchanged, relative to those of the g- and A matrices.

The spectrum observed at temperatures in the liquid helium region arises from transitions between the levels of the Sz = $\pm{}^1/_2$ Kramers doublet of the quartet state, which, since D is positive, lies lowest and is the only doublet with a significant spin population at 2.2 K. A negative D results in the Sz = $^3/_2$ doublet having a significant population at 2.2 K and exhibiting resonances at $g_z \approx 6$ (~1100 G) and at magnetic fields approaching those for which $g \approx 0$. These resonances are not observed. The effective g-values of the lowest doublet arising from the quartet state of a $S = {}^3/_2$ spin system derived from the coupling of three $S = {}^1/_2$ entities can be derived from the expressions of Banci et al.[51] for a linear, exchange-coupled trimer. Using the g-values for nitroxide radicals, estimated from the spectrum of a nitroxide radical in the analogous system $[Fe^{II}(L^{\bullet})_2](BF_4)_2$,[12] which are similar to those given by Dzuba,[52] we estimate the "real" g-values for the uncoupled low-spin Co (II) ion as g_x = 2.25, g_y = 2.14, and g_z = 1.97. These g-values are rather more in accordance with the expectation for low-spin Co(II) than those listed in Table 1 and are consistent with previous studies on a series of spin-crossover Co(II) alkyl chain terpyridine-based complexes.[53]

The characteristics of the spectra observed at temperatures between 2.2 K and 295 K depend on the spin-relaxation behavior of the individual components and the trimeric spin system as a whole. For low-spin Co(II) ions, spin−lattice relaxation effects generally result in line broadening above ~100 K, and these would appear to be the cause of the disappearance of the broad resonances at ~1700 G above 110 K. As discussed by Gatteschi,[6d] spin relaxation at higher temperatures can occur via the doublet states which become populated at these temperatures. The spin-crossover transition also introduces a gradually increasing population of high-spin Co(II) above 120 K. The short spin−lattice relaxation time of the Co(II) ion means that any resonances associated with it will be so broad that they would be unobservable at higher temperatures. The seemingly isotropic resonances at $g \approx 2.003$ observed in the high-temperature region (above 200 K) would appear to result from the averaging out of the anisotropic g- and hyperfine interactions of the nitroxide radicals, as a consequence of these spin-relaxation pathways.

3.4. Electrochemistry. Unlike the iron(II) complex, $[Fe^{II}(L^{\bullet})_2](BF_4)_2$,[12] EPR measurements on the conceptually and structurally related congener $[Co^{II}(L^{\bullet})_2](NO_3)_2$, **1** did not show any contribution arising from the mixed-valent $[Co^{III}(L^{\bullet})(L^{-})]^{2+}$ species, which can be formed, presumably, via an intramolecular metal-to-ligand charge-transfer reaction. Thus, in solution $[Co^{II}(L^{\bullet})_2]^{2+}$ (**1**) is likely to be the thermodynamically favored form, as is its oxidized form $[Co^{III}(L^{-})_2]^{+}$ (**2**). Clearly, electrochemical studies on **1** and **2** may provide details of the relationship between **1** and **2** in a redox sense, as was the case with the iron analogues where the reaction scheme was deduced to be as depicted in Scheme 1.[12]

Scheme 1. Square Scheme Depicting the Different Species Involved in the Redox Reaction of $[Fe^{II}(L^{\bullet})_2](BF_4)_2$.[12]

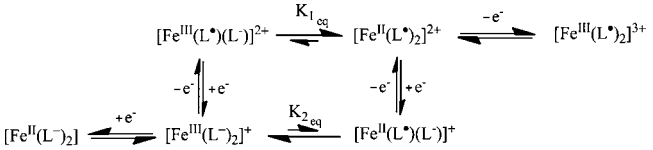

The voltammetry (Figure 10) of $[Co^{III}(L^{-})_2](BPh_4)$, (**2**), in acetonitrile (0.1 M $[Bu_4N](PF_6)$) at a 1.5 mm glassy carbon (GC) electrode under transient conditions (Figures 10a and c, scan rates = 20−200 mV s^{-1}) and near-steady-state conditions (Figure 10b, scan rate = 1 mV s^{-1}), resembles that reported for the $[Fe^{III}(L^{-})_2](BPh_4)$ congener, but exhibits some additional complexity.[12] Thus, four processes, labeled **I**, **II**, **III**, and **IV** in Figure 10 are found in the potential range of +1.0 V to −1.7 V vs $[FeCp_2]^{0/+}$ in this solvent. Other irreversible processes were detected outside this potential range (as also applies to **1**), but are not relevant to the theme of interest in this paper and, therefore, are not discussed. The transient cyclic voltammograms associated with the designated processes **I**, **II**, **III**, and **IV** in Figure 10a reveals that chemically irreversible process **IV**, which corresponds to the oxidation of $[BPh_4]^{-}$,[12] leads to difficulties in the analysis of process **I**, which occurs at a slightly more positive potential. Chemically reversible process **II** is diffusion-controlled, as evidenced by the linear dependence of both reduction and oxidation peak currents on the square root

dx.doi.org/10.1021/ic400565h | Inorg. Chem. 2013, 52, 7557−7572

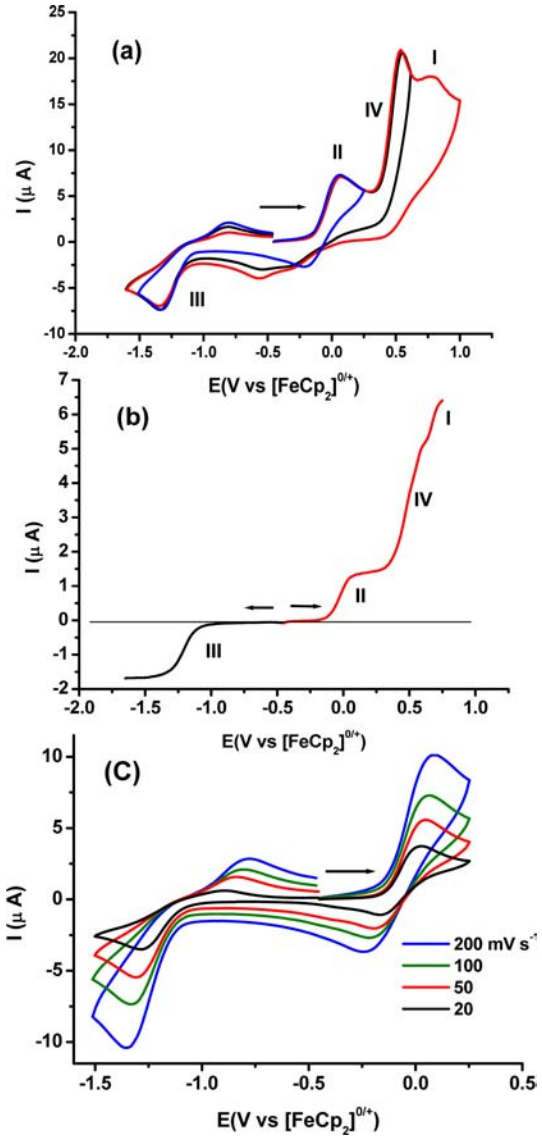

Figure 10. (a) Transient cyclic and (b) linear sweep near-steady-state voltammograms obtained with a 1.5-mm-diameter glassy carbon disk electrode, using scan rates of 100 and 1 mV s^{-1}, respectively, for ~1 mM **2** in CH_3CN (0.1 M $[Bu_4N](PF_6)$) at 298 K. (c) Cyclic voltammograms as a function of scan rate.

of the scan rate, whereas process **III**, while diffusion-controlled at the reduction peak potential, is chemically irreversible. Analysis of the relative magnitudes and signs of limiting currents and wave shapes associated with the slow-scan-rate near-steady-state current–potential voltammetric response at a slow scan rate of 1 mV s^{-1} at a glassy carbon macrodisk electrode in Figure 10b reveals that **2** gives rise to two one-electron oxidation processes **I** and **II** (current positive in Figure 10b) and one reduction process (current negative in Figure 10b), in addition to multielectron process **IV** associated with oxidation of the $[BPh_4]^-$ anion. Process **III** has a halfwave potential of $E_{1/2}$ = −1.22 V and is assigned to a metal-based Co(III)/Co(II) reduction step, as proposed in eq 2 to give the corresponding neutral $[Co^{II}(L^-)_2]$ product, which, unlike the iron analogue, is unstable on the voltammetric time scale.

$$[Co^{III}(L^-)_2]^+ \overset{+e^-}{\rightleftharpoons} [Co^{II}(L^-)_2] \overset{\text{fast}}{\longrightarrow} \text{products} \qquad (2)$$

The steady-state $E_{1/2}$ value for oxidation process **II** is −0.03 V, as is the midpoint potential (E_m) derived from cyclic voltammetry from the average of the oxidation and reduction peak potentials. By analogy, like the iron congener, this is assumed to occur as in square scheme 2, where K_{1eq} and K_{2eq}

Scheme 2. Square Scheme Depicting the Different Species Involved in the First Oxidation Step (Process II) of 2

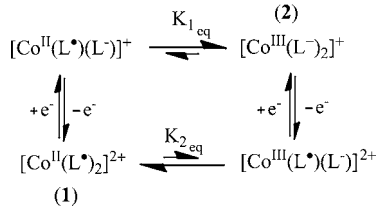

are equilibrium constants. Further evidence for this reaction will be provided below when the voltammetry of **1** is presented. Consequently, process **II** is ascribed mainly to the oxidation of one of the monoanionic forms of the oxazolidine–*N*-oxide ligands to yield $[Co^{III}(L^•)(L^-)]^{2+}$. This species then presumably undergoes rapid intramolecular ligand-to-metal charge transfer to form the thermodynamically favored $[Co^{II}(L^•)_2]^{2+}$ species (**1**), which contains the original radical form of the ligand. The cobalt(II) species, along with the equilibrium concentration of $[Co^{III}(L^•)(L^-)]^{2+}$, is further oxidized via process **I** ($E_{1/2}$ = 0.61 V), as in eq 3, to generate the tricationic cobalt(III) species, $[Co^{III}(L^•)_2]^{3+}$.

$$[Co^{II}(L^•)_2]^{2+} \overset{-e^-}{\rightleftharpoons} [Co^{III}(L^•)_2]^{3+} \qquad (3)$$

The voltammetry of complex **1** as a nitrate salt in acetonitrile (0.1 M $[Bu_4N](PF_6)$) is displayed in Figure S6 in the Supporting Information. Some of the characteristics predicted on the basis of the voltammetry of **2** and the relationships of their structures is evident, but also some additional features are observed. Since **1** is a nitrate salt, process **IV** arising from oxidation of $[BPh_4]^-$ present as the anion for **2**, is of course absent. This enables process **I** to be more readily studied in the case of **1** than **2**. Cyclic voltammetry at a GC macrodisk electrode now clearly reveals a well-defined chemically reversible, diffusion-controlled, one-electron oxidation step with E_m at +0.60 V (see Figures S6a and S6b in the Supporting Information), which corresponds to the reaction in eq 3, for both **1** and **2**. Process **II** for **1** also is well-defined, with E_m = −0.04 V, but the peak current is smaller than that for process **I**. Importantly, the steady-state voltammogram at a carbon fiber microelectrode in Figure S6c in the Supporting Information confirms that process **II**, which is derived from **1**, is now a reduction rather than oxidation step, as found for **2**. This is as expected on the basis of square scheme 3, which is the

Scheme 3. Square Scheme Depicting the Different Species Involved in the First Reduction Step (Process II) of 1

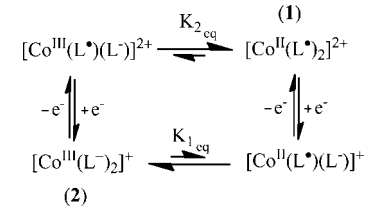

dx.doi.org/10.1021/ic400565h | Inorg. Chem. 2013, 52, 7557–7572

reduction counterpart of reaction scheme 2. Figure S6b in the Supporting Information reveals that the potential region, which is slightly more negative than process **II** in **1**, is now more complicated than when starting with **2**, because of the presence of processes **V** and **VI**. The steady-state response for process **V** has a nonsigmoidal peak shape, which suggests that precipitation or adsorption of a product has occurred so that this process corresponds to a surface confined rather than solution-phase reaction. Indeed, if the initial potential is held in the region of processes **V** and **VI**, then severe electrode fouling and blocking of processes **II** and **I** occurs. That is, the voltammetry observed on scanning in the positive potential direction is now poorly defined. Also noteworthy for **1** is that process **II**, in combination with process **V** (see Figures S6b and S6c in the Supporting Information), has a current magnitude corresponding to that for process **I** and, hence, represents the total of a one-electron reduction in a coulometric sense. It is likely that the nitrate anion is not innocent in the voltammetry of **1**. The analogue of irreversible process **III** reported for **2** is located at approximately −1.24 V (cyclic voltammetry scan rate 100 mV s^{-1}) in the case of **1**. This process, since it is derived in part from the reduction of products formed in processes **V** and **VI**, can be designated as process **VII** (not shown). In summary, the introduction of surface-confined electrochemistry in **1** modifies process **II** and, hence, all processes at more-negative potentials in a manner that does not apply to **2**. Nevertheless, the electrochemical data, despite being far more complex than that for the corresponding iron compound, where processes **I**, **II**, and **III** are all fully reversible,[12] does explain why the chemical oxidation of **1** leads to structurally rearranged **2** and vice versa, given that square reaction schemes are still operative.

Taken together, the voltammetric data for the two cobalt complexes, **1** and **2**, along with their iron analogues, clearly establish that the four members of this family essentially share inter-related voltammetric features, i.e., exhibit three one-electron processes, **I**, **II**, and **III**, with a square scheme providing chemical rearrangement with equilibrium constants K_{1eq} and K_{2eq} that couple two-electron transfer processes. As seen for the iron system, the redox chemistry of the cobalt compounds **1** and **2** underscores the fact that the oxazolidine–*N*-oxide ligand is a noninnocent ligand and is the main cause of the redox-induced structural changes associated with square reaction schemes 2 and 3. Very significant in this regard is the chemical synthesis of the monocations $[Co^{III}(L^-)_2]^+$ and $[Fe^{III}(L^-)_2]^+$ achieved from their parent $[Co^{II}(L^\bullet)_2]^{2+}$ and $[Fe^{II}(L^\bullet)_2]^{2+}$ complex via a fast, reductively induced intermolecular metal-to-ligand charge transfer that takes place upon one-electron reduction of the ligand. Table 5 provides a comparison of the reversible potentials for processes **I**, **II**, and **III** for the cobalt and iron congeners, and it shows that the differences are not very large.

3.5. Theoretical Studies. Experimental measurements suggest that the ground state for complex **1** is $S = {}^3/_2$; this can arise from several different spin-exchange coupled scenarios. The first scenario considered involves two radical ligands coupled ferromagnetically to the LS Co(II) ion and a simultaneous ferromagnetic superexchange between the two radical ligands mediated via the LS Co(II) ion and corresponds to the experimental observations ($^4\mathbf{1}_{LS}$). The second scenario involves a HS Co(II) case, where the two radical ligands are coupled ferromagnetically to each other with a weak antiferromagnetic coupling with the central Co(II) ion. A very strong radical–radical interaction ensures an $S = {}^3/_2$ ground state ($^4\mathbf{1}_{HS}$).

Table 5. Reversible Potentials (V vs $[FeCp_2]^{0/+}$) for Designated Processes I, II, and III Exhibited by the Fe and Co Complexes

	I	II	III	ref
$[Fe^{II}(L^\bullet)_2]^{2+}$	0.68	−0.10	−1.15	12
$[Fe^{III}(L^-)_2]^+$	0.68	−0.10	−1.15	12
$[Co^{II}(L^\bullet)_2]^{2+}$ (**1**)	0.60	−0.04	−1.24[a]	this work
$[Co^{III}(L^-)_2]^+$ (**2**)	0.62[a,b]	−0.03	−1.22[c]	this work

[a]An irreversible process is involved, so the peak potential value is given. [b]Overlap with $[BPh_4]^-$ oxidation process introduces significant uncertainty. [c]An irreversible process is involved, so the $E_{1/2}$ value is given.

Here, we have considered both the HS and LS Co(II) cases and extracted the exchange coupling for each to rationalize the observed magnetic behavior. The exchange interaction computed for the HS Co(II) case will be especially useful, because there are no experimental data on the type, sign, and magnitude of any possible exchange coupling due to difficulties in extracting such parameters in a system that has simultaneous spin-crossover, exchange, and temperature-dependent HS Co(II) behavior.

3.5.1. Structure and Energetics. Structure optimizations were performed for configurations $^4\mathbf{1}_{LS}$ and $^4\mathbf{1}_{HS}$ (see Table S1 in the Supporting Information for the computed spin-density values), and the computed structural parameters for configurations $^4\mathbf{1}_{LS}$ and $^4\mathbf{1}_{HS}$ are given in Figure 11. Although some structural parameters are overestimated, compared to the experimental structural parameters,[55] it is apparent from the given selected structural parameters that structure $^4\mathbf{1}_{LS}$ is a better match to the experimental structure determined at 123 K (see Figure 11) while $^4\mathbf{1}_{HS}$ corresponds to the structure determined at 353 K (see Figure 3 for experimental bond lengths). Also, $^4\mathbf{1}_{LS}$ is expected to have a pseudo-Jahn–Teller distortion and the computed structure nicely reproduces this distortion along the O–Co–O vector, as seen in the X-ray structure. For configuration $^4\mathbf{1}_{HS}$, computations reveal larger metal–ligand bond lengths as expected for high-spin Co(II) complexes.

For comparison, computation has also been performed on the sextet state ($^6\mathbf{1}_{HS}$) corresponding to ferromagnetic exchange between both the radical ligands and HS Co(II). Calculations reveal that $^4\mathbf{1}_{LS}$ is the ground state with $^6\mathbf{1}_{HS}$ and $^4\mathbf{1}_{HS}$ lying 1.1 and 5.6 kJ/mol higher in energy, respectively. Our energetics confirm that $^4\mathbf{1}_{LS}$ is the ground state and this is consistent with the experimental observation of an $S = {}^3/_2$ ground state at low temperature, resulting from a strong ferromagnetic interaction between the LS Co(II) ion and the radical ligand spins.

3.5.2. Magnetic Exchange. The exchange parameters have been computed on the X-ray structure assuming (a) Co(II) in the LS state and (b) Co(II) in the HS state. Two different exchange interactions have been assumed based on the spin Hamiltonian $\hat{H} = -2J_1(\hat{S}_1\cdot\hat{S}_2 + \hat{S}_2\cdot\hat{S}_3) - 2J_2(\hat{S}_1\cdot\hat{S}_3)$ (where S_1 and S_3 are for the radicals and S_2 is for the Co^{II} ion). For configuration $^4\mathbf{1}_{LS}$, the parameter set $J_1 = +67.3$ cm^{-1} and $J_2 = +15.1$ cm^{-1} has been obtained. This gives rise to an $S = {}^3/_2$ ground state with two $S = {}^1/_2$ levels at 97.5 cm^{-1} and 201.9 cm^{-1}, respectively. Although the estimate of J_1 matches with the experimental (susceptibility) data, the magnitude of J_2 is

dx.doi.org/10.1021/ic400565h | Inorg. Chem. 2013, 52, 7557–7572

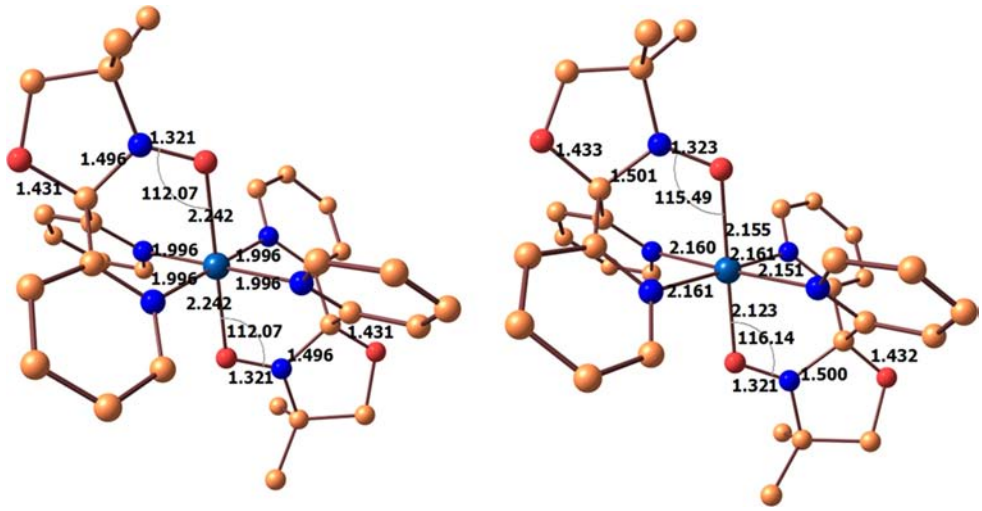

Figure 11. B3LYP optimized structures for configurations (a) $^4\mathbf{1}_{LS}$ and (b) $^4\mathbf{1}_{HS}$, along with selected structural parameters. Bond lengths are given in Ångstroms and bond angles are given in degrees.

computed to be smaller than J_1 and, here, our data deviates from the experimental estimates. For HS Co(II), the exchange interactions between the metal and the radical centers are antiferromagnetic (AF) and weak in nature, with $J_1 = -5$ cm^{-1}, whereas the radical−radical interaction is computed to be large and ferromagnetic, with $J_2 = +109.7$ cm^{-1}. This leads to an effective ground state of $S = {}^1/_2$. With these estimates, the first excited $S = {}^3/_2$ state lies 15.0 cm^{-1} above the ground state. The remaining $S = {}^5/_2$ and $S = {}^3/_2$ states lie 40 cm^{-1} and 244 cm^{-1} above the ground state, respectively. We have previously reported a strong AF radical−radical super exchange in the $[Fe^{II}(L^{\bullet})_2](BF_4)_2$ complex,[12] so the strong ferromagnetic interaction calculated is not without precedent and implies a large orbital overlap between the magnetic orbitals in the HS Co(II) ion and the π^*_{NO} orbital of the ligand. Computation of the J parameters on the optimized geometries also yield a similar trend −albeit despite the fact that the magnitudes of the J parameters are diminished (see Table S2 in the Supporting Information).

The magnetic exchange of LS Co(II) with the radicals, and the radical−radical super exchange via the LS Co(II), are computed to be ferromagnetic for $^4\mathbf{1}_{LS}$ while, for $^4\mathbf{1}_{HS}$, the computed HS Co(II)−radical exchange is AF and the radical−radical super exchange via the HS Co(II) is strongly ferromagnetic. To probe the origin of this interaction further, we have analyzed the electronic structure of these two species. The magnetic orbitals of $^4\mathbf{1}_{LS}$ and $^4\mathbf{1}_{HS}$ are shown in Figure 12, along with their computed energies. Our calculations on the $^4\mathbf{1}_{LS}$ configuration clearly reveal that the unpaired electron in Co(II) is located in the d_{z^2} orbital (see Figure 13), while the radical unpaired electrons are located in the π^*_{NO} orbitals, which are perpendicular to the five-membered ring of the radical ligand. As evident from Figure 12a, the d_{z^2} orbital of Co(II) is orthogonal to the π^*_{NO} orbital(s) of the nitroxide ligand, yielding a ferromagnetic coupling between the radical and the LS Co(II) center. The two radical π^*_{NO} orbitals are aligned parallel to each other with a very small overlap expected between them. This leads to ferromagnetic coupling between radical centers. These qualitative arguments are also supported by overlap integrals computed between the MOs (see see Table S3 in the Supporting Information).

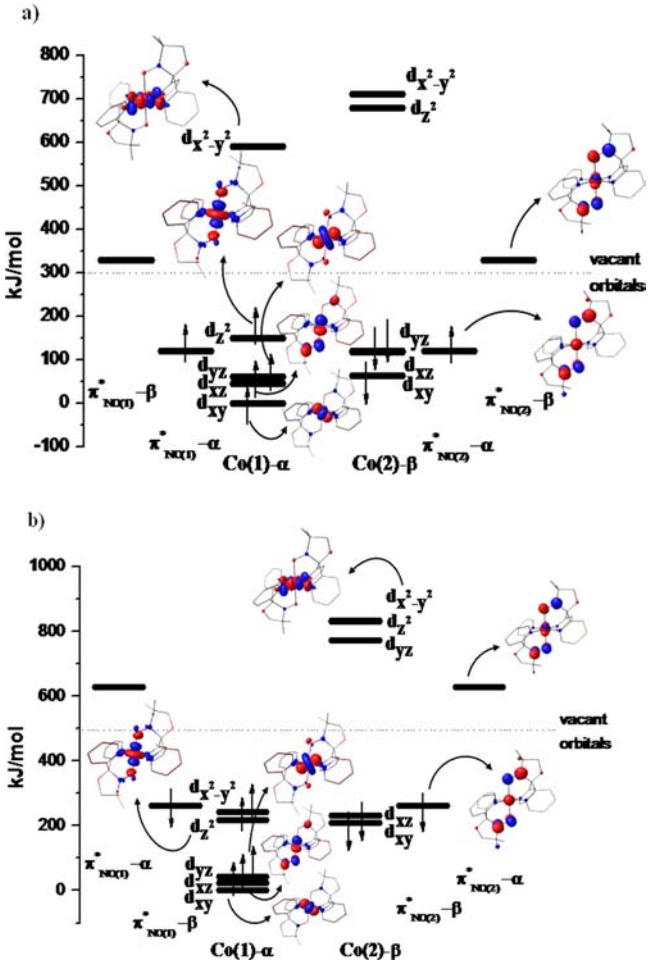

Figure 12. Eigenvalue plots of the LS Co(II) and radical ligands along with the DFT computed energies for the (a) $^4\mathbf{1}_{LS}$ and (b) $^4\mathbf{1}_{HS}$ configurations.

The computed orbital diagram for the $^4\mathbf{1}_{HS}$ configuration is shown in Figure 12b. For the HS Co(II) ion the following electronic configuration was determined: $(d_{xy})^2(d_{xz})^2(d_{yz})^1(d_{z^2})^1(d_{x^2-y^2})^1$. As evidenced by Figure 12b, the unpaired electron in the t_{2g} set is in the d_{yz} orbital, which

dx.doi.org/10.1021/ic400565h | Inorg. Chem. 2013, 52, 7557−7572

interacts with the symmetry compatible π^*_{NO} orbitals. The energy spacing between these two magnetic orbitals is large, leading to a small overlap between the d_{yz} and π^*_{NO} orbitals, resulting in a weak AF interaction between the HS Co(II) ion and the radical centers. On the other hand, the π^*_{NO} orbitals, which lie parallel to each other, interact rather strongly. A weak overlap between the π^*_{NO} orbital and the d_{yz} orbital of the Co(II) ion promotes a polarization mechanism that leads to strong ferromagnetic coupling between two radical centers. A comparison between the radical −LS Co(II) and radical −HS Co(II) interactions are shown in Scheme 4.

Scheme 4. Illustrative Molecular Orbital (MO) Diagram Depicting the Significant Interactions between Radical and Co(II) Center When Considering Low-Spin (LS) (Left) and High-Spin (HS) (Right) States of Co(II) in 1

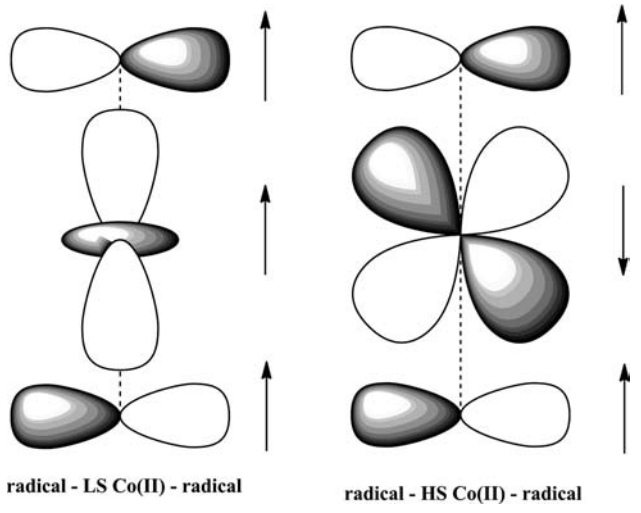

Computed spin density plots for $^4\mathbf{1}_{LS}$ and $^4\mathbf{1}_{HS}$ are shown in Figure 13. For $^4\mathbf{1}_{LS}$, the d_z^2 orbital shape of Co(II) is very clear

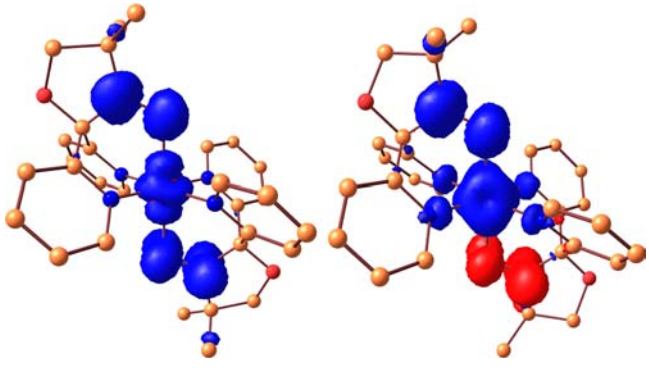

Figure 13. DFT computed spin density for the $^4\mathbf{1}_{LS}$ (left) and $^4\mathbf{1}_{HS}$ (right) configurations. Blue represents spin up, and red represents spin down.

from the spin density plot and the radical spin densities are equally distributed to O and N atoms, with nitrogen possessing slightly larger values (0.483 on oxygen vs 0.524 on nitrogen). The spin density on the LS Co(II) ion is 1.012, suggesting that spin delocalization is not prominent. For the $^4\mathbf{1}_{HS}$ state, a cubic shape was detected with a spin density of 2.74, revealing significant spin delocalization. On the radical centers, a spin density of −0.378 on the oxygen and −0.552 on the nitrogen was estimated. The estimated spin density on the oxygen atoms are much lower than that of the $^4\mathbf{1}_{LS}$ configuration, indicating that, along the O−Co−O direction, there is some spin polarization, as suggested earlier with the HS case. (See Table S1 in the Supporting Information for computed spin-density values.)

To validate our computed J values, we have calculated the molar magnetic susceptibility using the HS and LS Co(II) DFT computed values. Since spin crossover has been observed for complex **1**, the molar magnetic susceptibility of the complex at a particular temperature would have contributions from both LS and HS states of the metal ion, depending on their relative abundance (mole fraction) at that temperature. The HS mole fraction (x) can be calculated using the following equation[56] at a temperature T (given in Kelvin) and, thereby, the mole fraction for LS would be of $(1 - x)$.

$$x = \frac{\chi T - (\chi T)\mathrm{LS}}{(\chi T)\mathrm{HS} - (\chi T)\mathrm{LS}}$$

Taking the DFT estimated values and assuming a g-value of 2.0 for both spin states, the above equations yield a susceptibility curve that is strikingly similar to that of the experiment (see Figure 14). Particularly, the shape of the curve

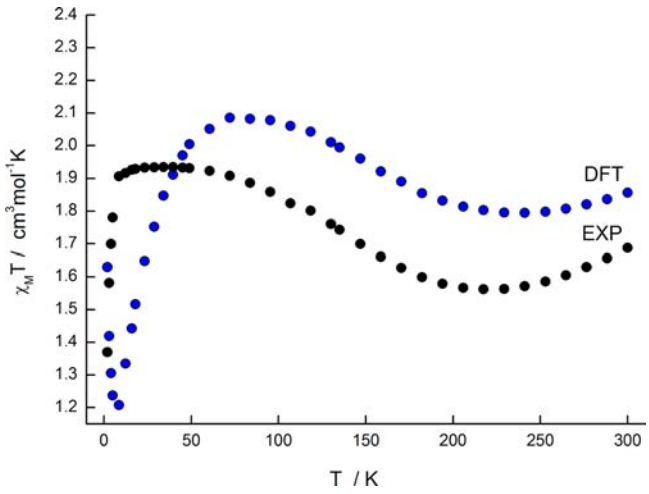

Figure 14. Plot of $\chi_M T$ vs T for **1** between 2 K and 300 K in (black circles). The blue circles are DFT calculated points (see text for details).

is very well reproduced. Given the fact that there are numerous parameters involved, we have not attempted to fit the experimental data, but this simulation adds confidence to the computed results and suggests how the coupling between the radical centers can be tuned by the nature of the spin state at the metal center.

4. CONCLUSIONS

The two related complexes of the nitroxide chelating ligand, $[Co^{II}(L^{\bullet})_2](NO_3)_2$ (**1**) and $[Co^{III}(L^{-})_2](BPh_4)$ (**2**), have been synthesized and structurally characterized. The Co ions in **1** and **2** display an octahedral geometry formed by equatorial coordination of four nitrogens and axial coordination from two oxygens of the radical ligand, forming a linear $L^{\bullet/-}\cdots Co^{II/III}\cdots L^{\bullet/-}$ arrangement. The cations in **1** and **2** are structurally similar but vary in regard to a few significant bond lengths and angles. Complex **1**, $[Co^{II}(L^{\bullet})_2](NO_3)_2$, contains

dx.doi.org/10.1021/ic400565h | Inorg. Chem. 2013, 52, 7557−7572

the neutral radical form, $L^{\bullet}$, with the cobalt in the low-spin Co(II) state at low temperatures and undergoes a thermally induced gradual spin crossover to the high-spin Co(II) state. Complex **2**, $[Co^{III}(L^{-})_2](BPh_4)$, contains the reduced form, L^{-}, of the ligand with the cobalt in the low-spin Co(III) state throughout the temperature range studied. The existence of the cobalt spin/oxidation states and neutral or anionic form of the ligand has been characterized by structural, solid-state magnetic susceptibility, and EPR spectroscopic studies and confirmed by DFT calculations. Electrochemical studies support the existence of **1** and **2** in solution and the interplay between the redox states of **1** and **2** are fully described with the use of square schemes. Complex **1** shows strong radical-cobalt and radical−radical ferromagnetic interactions below 200 K stabilizing a $S = {}^3/_2$ ground state with ac susceptibility measurements confirming field-induced slow magnetic relaxation effects. Complex **2** is formed by a "reductively induced oxidation" of the central cobalt ion by use of the tetraphenylborate anion and it is diamagnetic over the temperature range studied.

The most important and significant feature of complex **1** is that it is a rare, if not unique, example of a hybrid molecular magnetic material that displays the multiple functions of spin-crossover, intramolecular ferromagnetic exchange, single-molecule magnetism, and metal−ligand redox processes. Such materials are of much current interest in developing nanomaterials therefrom and exploring both fundamental and applied properties. The redox-active features of such metal-radical compounds can also lead to applications in organic reactivity and catalysis.[57]

■ ASSOCIATED CONTENT

Supporting Information

Crystallographic data as .cif files. Figures S1 and S2 are molecular structure pictures; Figures S3−S5 are magnetism plots; Figure S6 shows electrochemical voltammograms; Tables S1−S5 give computational (DFT) data. This material is available free of charge via the Internet at http://pubs.acs.org.

■ AUTHOR INFORMATION

Corresponding Author

*E-mail: keith.murray@monash.edu.

Notes

The authors declare no competing financial interest.

■ ACKNOWLEDGMENTS

K.S.M. acknowledges the support of an Australian Research Council Discovery grant and, with G.R., the support of an Australia-India Strategic Research Fund grant.

■ REFERENCES

(1) See articles in: *Dithiolene Chemistry: Synthesis, Properties and Applications*; Karlin, K. D., Stiefel, E. I., Eds.; Progress in Inorganic Chemistry, Vol. *52*; Wiley: Hoboken, NJ, 2003.

(2) (a) Kaim, W.; Reinhardt, R.; Sieger, M. *Inorg. Chem.* **1994**, *33*, 4453. (b) Záliš, S.; Sieger, M.; Greulich, S.; Stoll, H.; Kaim, W. *Inorg. Chem.* **2003**, *42*, 5185. (c) Sieger, M.; Kaim, W.; Stufkens, D. J.; Snoeck, T. L.; Stoll, H.; Záliš, M. *Dalton Trans.* **2004**, 3815. (d) Ray, K.; Petrenko, T.; Wieghardt, K.; Neese, F. *Dalton Trans.* **2007**, 1552. (e) Khusniyarov, M. M.; Weyhermüller, T.; Bill, E.; Wieghardt, K. *J. Am. Chem. Soc.* **2009**, *131*, 1208.

(3) (a) Pierpont, C. G.; Lange, C. W. *Prog. Inorg. Chem.* **1994**, *41*, 331. (b) Pierpont, C. G. *Coord. Chem. Rev.* **2001**, *95*, 216. (c) Griffith, W. P. *Trans. Met. Chem.* **1993**, *18*, 250. (d) Bhattacharya, S.; Gupta, P.; Basuli, F.; Pierpont, C. G. *Inorg. Chem.* **2002**, *41*, 5810. (e) Haga, M.; Dodsworth, E. S.; Lever, A. B. P. *Inorg. Chem.* **1986**, *25*, 447. (f) Kalinina, D.; Dares, C.; Kaluarachchi, H.; Potvin, P. G.; Lever, A. B. P. *Inorg. Chem.* **2008**, *47*, 10110.

(4) Kaim, W.; Schwederski, B. *Coord. Chem. Rev.* **2010**, *254*, 1580. (b) Kaim, W. *Eur. J. Inorg. Chem.* **2012**, 343.

(5) Burgmayer, S. J. N.; Pearsall, D. L.; Blaney, S. M.; Moore, E. M.; Sauk-Schubert, C. *J. Biol. Inorg. Chem.* **2004**, *9*, 59.

(6) (a) Okazawa, A.; Hashizume, D.; Ishida, T. *J. Am. Chem. Soc.* **2010**, *132*, 11516. (b) Vostrikova, K. E. *Coord. Chem. Rev.* **2008**, *252*, 1409. (c) Caneschi, A.; Gatteschi, D.; Rey, P. *Prog. Inorg. Chem.* **1991**, *39*, 331. (d) Bencini, A.; Gatteschi, D. *EPR of Exchange Coupled Systems*; Springer−Verlag: Berlin, Heidelberg, 1990. (e) Caneschi, A.; Gatteschi, D.; Sessoli, R. *Acc. Chem. Res.* **1989**, *22*, 392.

(7) Kaim, W. *Inorg. Chem.* **2011**, *50*, 9752.

(8) Caneschi, A.; Gatteschi, D.; Grand, A.; Laugier, J.; Pardi, L.; Rey, P. *Inorg. Chem.* **1988**, *27*, 1031.

(9) Luneau, D.; Rey, P.; Laugier, J.; Fries, P.; Caneschi, A.; Gatteschi, D.; Sessoli, R. *J. Am. Chem. Soc.* **1991**, *113*, 1245.

(10) Ito, A.; Nakano, Y.; Urabe, M.; Tanaka, K.; Shiro, M. *Eur. J. Inorg. Chem.* **2006**, 3359.

(11) Dickman, M. H.; Porter, L. C.; Doedens, R. J. *Inorg. Chem.* **1986**, *25*, 2595.

(12) Gass, I. A.; Gartshore, C. J.; Lupton, D. W.; Moubaraki, B.; Nafady, A.; Bond, A. M.; Boas, J. F.; Cashion, J. D.; Milsmann, C.; Wieghardt, K.; Murray, K. S. *Inorg. Chem.* **2011**, *50*, 3052.

(13) (a) Sheldrick, G. M. SHELXL-97. In *Program for Refinement of Crystal Structures*, University of Göttingen, Germany, 1997. (b) Spek, A. L. *Acta Crystallogr., Sect. A: Found. Crystallogr.* **1990**, *46*, C34.

(14) Wertz, J. E.; Orton, J. W.; Auzins, P. *Faraday Discuss.* **1961**, *31*, 140.

(15) (a) Hanson, G. R.; Gates, K. E.; Noble, C. J.; Griffin, M.; Benson, S. *J. Inorg. Biochem.* **2004**, *98*, 903.

(16) *Introduction to Computational Chemistry*, 2nd Ed.; Jensen, F.; John Wiley & Sons, Ltd.: Chichester, U.K., 2007.

(17) Frisch, M. J.; Trucks, G. W.; Schlegel, H. B.; Scuseria, G. E.; Robb, M. A.; Cheeseman, J. R.; Scalmani, G.; Barone, V.; Mennucci, B.; Petersson, G. A.; Nakatsuji, H.; Caricato, M.; Li, X.; Hratchian, H. P.; Izmaylov, A. F.; Bloino, J.; Zheng, G.; Sonnenberg, J. L.; Hada, M.; Ehara, M.; Toyota, K.; Fukuda, R.; Hasegawa, J.; Ishida, M.; Nakajima, T.; Honda, Y.; Kitao, O.; Nakai, H.; Vreven, T.; Montgomery, J. A.; Peralta, Jr. J. E.; Ogliaro, F.; Bearpark, M.; Heyd, J. J.; Brothers, E.; Kudin, K. N.; Staroverov, V. N.; Kobayashi, R.; Normand, J.; Raghavachari, K.; Rendell, A.; Burant, J. C.; Iyengar, S. S.; Tomasi, J.; Cossi, M.; Rega, N.; Millam, J. M.; Klene, M.; Knox, J. E.; Cross, J. B.; Bakken, V.; Adamo, C.; Jaramillo, J.; Gomperts, R.; Stratmann, R. E.; Yazyev, O.; Austin, A. J.; Cammi, R.; Pomelli, C.; Ochterski, J. W.; Martin, R. L.; Morokuma, K.; Zakrzewski, V. G.; Voth, G. A.; Salvador, P.; Dannenberg, J. J.; Dapprich, S.; Daniels, A. D.; Farkas, Ö.; Ortiz, J. V.; Cioslowski, J.; Fox, D. J. *Gaussian 09, Revision A.01*, Wallingford, CT, 2009.

(18) Noodleman, L.; Peng, C. Y.; Case, D. A.; Mouesca, J. M. *Coord. Chem. Rev.* **1995**, *144*, 199.

(19) (a) Becke, A. D. *J. Chem. Phys.* **1986**, *84*, 4524. (b) Perdew, J. P. *Phys. Rev. B.* **1986**, *33*, 8822.

(20) Berg, N.; Rajeshkumar, T.; Taylor, S. M.; Brechin, E. K.; Rajaraman, G.; Jones, L. F. *Chem.—Eur. J.* **2012**, *18*, 5906.

(21) (a) Rajeshkumar, T.; Singh, S. K.; Rajaraman, G. *Polyhedron* **2013**, *52*, 1299. (b) Singh, S. K.; Neeraj, K. T.; Rajaraman, G. *Dalton Trans* **2011**, *40*, 10897. (c) Rajeshkumar, T.; Rajaraman, G. *Chem. Commun.* **2012**, *48*, 7856. (d) Singh, S. K.; Rajaraman, G. *Dalton Trans.* **2013**, *42*, 3612.

(22) Cremades, E.; Gomez-Coca, S.; Aravena, D.; Alvarez, S.; Ruiz, E. *J. Am. Chem. Soc.* **2012**, *134*, 10532.

(23) (a) Tewary, S.; Gass, I. A.; Murray, K. S.; Rajaraman, G. *Eur. J. Inorg. Chem.* **2013**, 1024. (b) Paulsen, H.; Duelund, L.; Winkler, H.; Toftlund, H.; Trautwein, A. X. *Inorg. Chem.* **2001**, *40*, 2201. (c) Paulsen, H.; Paulsen, H.; Zimmermann, A.; Averseng, F.; Gerdan, M.; Winkler, H.; Toftlund, H.; Trautwein, A. X. *Monatsh.*

Chem. **2003**, *134*, 295. (d) Kripovic, I., K.; Zerara, M.; Daku, M. L.; Vargas, A.; Enachescu, C.; Ambrus, C.; Tregenna-. Piggott, P.; Amstutz, N.; Krausz, E.; Hauser, A. *Coord. Chem. Rev.* **2007**, *251*, 364.
(24) (a) Schafer, A.; Horn, H.; Ahlrichs, R. *J. Chem. Phys.* **1992**, *97*, 2571. (b) Schafer, A.; Huber, C.; Ahlrichs, R. *J. Chem. Phys.* **1994**, *100*, 5829.
(25) Molekel, Advanced Interactive 3D-Graphics for Molecular Sciences; available via the Internet at http:\\www.cscs.ch/molkel/. Version 1.6(build 338), Programming Zhurko, G.A.; available via the Internet at www.chemcraftprog.com.
(26) Tomasi, J.; Mennucci, B.; Cammi, R. *Chem. Rev.* **2005**, *105*, 2999−3093.
(27) Wong, M. A.; Frisch, M. J.; Wiberg, K. B. *J. Am. Chem. Soc.* **1991**, *113*, 4776.
(28) Wong, M. A.; Frisch, M. J.; Wiberg, K. B. *J. Am. Chem. Soc.* **1992**, *114*, 523.
(29) (a) Borrás-Almenar, J. J.; Clemente-Juan, J. M.; Coronado, E.; Tsukerblat, B. S. *Inorg. Chem.* **1999**, *38*, 6081. (b) Borrás-Almenar, J. J.; Clemente-Juan, J. M.; Coronado, E.; Tsukerblat, B. S. *J. Comput. Chem.* **2001**, *22*, 985.
(30) Nafady, A.; O'Mullane, A. P.; Bond, A. M.; Neufeld, A. K. *Chem. Mater.* **2006**, *18*, 4375.
(31) Geiger, W. E. In *Laboratory Techniques in Electrochemistry*, 2nd Edition; Kissinger, P. T., Heineman, W. R., Eds.; Marcel Dekker: New York, 1996; Chapter 23.
(32) Schomaker, V.; Trueblood, K. N. *Acta Crystallogr., Sect. B: Struct. Crystallogr. Cryst. Chem.* **1968**, *24*, 63.
(33) Goodwin, H. A. *Top. Curr. Chem.* **2004**, *234*, 23.
(34) Fujino, M.; Hasegawa, S.; Akutsu, H.; Yamada, J.; Nakatsuji, S. *Polyhedron* **2007**, *26*, 1989.
(35) Porter, L. C.; Doedens, R. J. *Inorg. Chem.* **1985**, *24*, 1007.
(36) Porter, L. C.; Dickman, M. H.; Doedens, R. J. *Inorg. Chem.* **1986**, *25*, 678.
(37) Matsunaga, P. T.; McCall, D. T.; Carducci, M. D.; Doedens, R. J. *Inorg. Chem.* **1990**, *29*, 1655.
(38) Porter, L. C.; Dickman, M. H.; Doedens, R. J. *Inorg. Chem.* **1988**, *27*, 1548.
(39) Kinoshita, H.; Akutsu, H.; Yamada, J.-I.; Nakatsuji, S. *Inorg. Chim. Acta* **2008**, *361*, 4159.
(40) Dickman, M. H. *Acta Crystallogr., Sect. C: Cryst. Struct. Commun.* **1997**, *53*, 1192.
(41) Ahlers, C.; Dickman, M. H. *Inorg. Chem.* **1998**, *37*, 6337.
(42) Jaitner, P.; Huber, W. *J. Organomet. Chem.* **1983**, *259*, C1.
(43) Jaitner, P.; Huber, W.; Gieren, A.; Betz.. *J. Organomet. Chem.* **1986**, *311*, 379.
(44) Chilton, N. F.; Anderson, R. P.; Turner, L. D; Soncini, A.; Murray, K. S. *J. Comput. Chem.* **2013**, *34*, 1164−1175.
(45) See, for example: Griffith, J. S. *Struct. Bonding (Berlin)* **1972**, *10*, 87. Jotham, R. W.; Kettle, S. F. A. *Inorg. Chim. Acta* **1970**, *4*, 145.
(46) (a) Vallejo, J.; Castro, I.; Ruiz-Garcia, R.; Cano, J.; Julve, M.; Lloret, F.; De Munno, G.; Wernsdorfer, W.; Pardo, E. *J. Am. Chem. Soc.* **2012**, *134*, 15704. (b) Feng, X.; Liu, J.; Harris, D.; Hill, S.; Long, J. R. *J. Am. Chem. Soc.* **2012**, *134*, 7521. (c) Karasawa, S.; Yoshihara, D.; Watanabe, N.; Nakano, M.; Koga, N. *Dalton Trans.* **2008**, 1418. (d) Zadrozny, J. M.; Liu, J.; Piro, N. A.; Chang, C. J.; Hill, S.; Long, J. R. *Chem. Commun.* **2012**, *48*, 3927. (e) Sanakis, Y.; Pissas, M.; Krzystek, J.; Telser, J.; Raptis, R. G. *Chem. Phys. Lett.* **2010**, *493*, 185. (f) Kajiwara, T.; Nakano, M.; Kaneko, Y.; Takaishi, S.; Ito, T.; Yamashita, M.; Igashira-Kamiyama, A.; Nojiri, H.; Ono, Y.; Kojima, N. *J. Am. Chem. Soc.* **2005**, *127*, 10150. (g) Tancini, E.; Rodriguez-Douton, M. J.; Sorace, L.; Barra, A.-L.; Sessoli, R.; Cornia, A. *Chem.—Eur. J.* **2010**, *16*, 10482.
(47) Krivokapic, I.; Zerara, M.; Daku, M. L.; Vargas, A.; Enachescu, C.; Ambrus, C.; Tregenna-Piggott, P.; Amstutz, N.; Krausz, E.; Hauser, A. *Coord. Chem. Rev.* **2007**, *251*, 364.
(48) Abragam, A.; Bleaney, B. *Electron Paramagnetic Resonance of Transition Ions*; Clarendon Press: Oxford, U.K., 1970; pp 447 and 751−752.
(49) Kremer, S.; Henke, W.; Reinen, D. *Inorg. Chem.* **1982**, *21*, 3013. Pilbrow, J. R. *Transition Ion Electron Paramagnetic Resonance*; Clarendon Press: Oxford, U.K., 1990; p 148.
(50) Makinen, M. W.; Kuo, L. C.; Yim, M. B.; Wells, G. B.; Fukuyama, J. M.; Kim, J. E. *J. Am. Chem. Soc.* **1985**, *107*, 5245.
(51) Banci, L.; Bencini, A.; Gatteschi, D. *Inorg. Chem* **1983**, *22*, 2681.
(52) Dzuba, S. A. *Phys. Lett. A* **1996**, *213*, 77. A simulation of the nitroxide radical spectrum published in ref gave g_x = 2.009, g_y = 2.006, g_z = 2.002. (From J. F. Boas, unpublished data.)
(53) Nielsen, P.; Toftlund, H.; Bond, A. D.; Boas, J. F.; Pilbrow, J. R.; Hanson, G. R.; Noble, C.; Riley, M. J.; Neville, S. M.; Moubaraki, B.; Murray, K. S. *Inorg. Chem.* **2009**, *48*, 7033.
(54) Pilbrow, J. R. *J. Magn. Reson.* **1978**, *31*, 479.
(55) Vargas, A.; Zerara, M.; Krausz, E.; Hauser, A.; Daku, L. M. L. *J. Chem. Theory Comput.* **2006**, *2*, 1342−1359.
(56) Kahn, O. *Molecular Magnetism*; VCH Publishers: New York, 1993. (ISBN: 1-56081-566-3.)
(57) Darmon, J. M.; Stieber, S. Ch. E.; Sylvester, K. T.; Fernández, I.; Lobkovsky, E.; Semproni, S. P.; Bill, E.; Wieghardt, K.; DeBeer, S.; Chirik, P. J. *J. Am. Chem. Soc.* **2012**, *134*, 1725.